ARCHITECTURE AND ASSEMBLY MECHANISM OF HUMAN LACTB

Jeremy A. Bennett[1], Lottie R. Steward[1], Johannes Rudolph[1], Adam P. Voss[1] and Halil Aydin[1,✉]

[1]Department of Biochemistry, University of Colorado Boulder, Boulder, CO 80309, USA

✉e-mail: halil.aydin@colorado.edu

ABSTRACT

Mitochondria are complex organelles that play a central role in metabolism. Dynamic membrane-associated processes regulate mitochondrial morphology and biogenesis in response to cellular demand. In tumor cells, metabolic reprogramming requires active mitochondrial metabolism for providing key metabolites and building blocks for tumor growth and rapid proliferation. To counter this, the mitochondrial serine beta-lactamase-like protein (LACTB) alters mitochondrial lipid metabolism and potently inhibits the proliferation of a variety of tumor cells. Mammalian LACTB is localized in the mitochondrial intermembrane space, where it assembles into filaments to regulate mitochondrial membrane organization and the efficiency of essential metabolic processes. However, the structural basis of LACTB polymerization and regulation remains incompletely understood. Here, we describe how human LACTB self-assembles into micron-scale filaments that increase their catalytic activity. The electron cryo-microscopy (cryoEM) structure defines the mechanism of assembly and reveals how highly ordered filament bundles stabilize the active state of the enzyme. We identify and characterize residues that are located at the filament-forming interface, and further show that mutations that disrupt filamentation reduce enzyme activity. Furthermore, our results provide evidence that LACTB filaments can bind lipid membranes. These data reveal the detailed molecular organization and polymerization-based regulation of human LACTB and provide new insights into the mechanism of mitochondrial membrane organization that modulates tumor suppression.

INTRODUCTION

Mitochondria are essential components of eukaryotic cells that communicate cellular needs to ensure optimal cellular function[1]. Although mitochondria play a critical role in energy production, mitochondrial metabolism is multifaceted and supports a variety of cellular functions, including free radical production, ion homeostasis, and biosynthesis of precursors for macromolecules[2]. Unlike most organelles, mitochondria are composed of two membranes: an outer membrane (OM) that interfaces directly with the cytosol, and a morphologically complex inner membrane (IM). The inner membrane separates the intermembrane space (IMS) from the matrix, and folds inwards to form cristae[3,4]. This complex double-membrane architecture provides discrete compartments for mitochondria to perform diverse metabolic functions[3]. In addition to their central role in various biochemical pathways, mitochondria are remarkably dynamic organelles that constantly adopt a range of morphologies and are actively transported to specific subcellular locations in response to cellular stressors[5,6].

Mitochondria are a major site for lipid metabolism, where biosynthesis of the phospholipids such as phosphatidylethanolamine (PE), phosphatidylglycerol (PG), and cardiolipin (CL) as well as redox-active lipid coenzyme Q (CoQ, ubiquinone) are facilitated by mitochondrial proteins and protein complexes[7–9]. Mitochondrial lipids are involved in maintaining mitochondrial morphology, cristae development, organelle dynamics, regulation of membrane-associated proteins, mitophagy and regulated cell death[10,11]. The key phospholipid PE is synthesized *de novo* by phosphatidylserine decarboxylase (PISD), a mitochondrial IM enzyme that converts phosphatidylserine (PS) to PE[11]. The newly synthesized PE is then exported to endoplasmic reticulum (ER) for further conversion to phosphatidylcholine (PC), the most abundant membrane lipid in eukaryotic cells[11]. Disruption of the orthologous gene *Pisd* in mouse models result in embryonic lethality associated with mitochondrial dysfunction and aberrant mitochondrial

morphology[12–14]. Hence, *de novo* synthesis of PE is essential for the efficiency of many subcellular processes and compartmentalization[11].

In many cancer cells, altered lipid metabolism is among the most prominent metabolic alterations that promotes rapid cancer cell growth and tumor formation[15]. Processes that regulate lipid levels are important targets for differentiation and proliferation of cancer cells[15]. Being at the junction of various metabolic pathways, mitochondrial processes are also associated with tumorigenesis and tumor progression[16]. Although mitochondrial dysfunction and aerobic glycolysis have been widely accepted as hallmarks of cancer, functional mitochondria are also important for tumor growth as active mitochondrial lipid metabolism supports the metabolic needs of highly proliferative cancer cells throughout tumorigenesis[16,17]. Conversely, tumor suppressor proteins can influence the production of lipids by acting through their biosynthesis pathway[18–22]. In mitochondria, the serine beta-lactamase-like protein (LACTB), which is localized in mitochondrial IMS, functions as a tumor suppressor by regulating the PE biosynthetic pathway[18,23,24]. While the direct mechanism for tumor suppression by LACTB is unknown, studies have shown that LACTB expression results in reduced PISD protein levels in human breast cancer cells[18]. Downregulation of PISD by LACTB is associated with markedly reduced production of PE from PS in carcinoma cells and decrease in cell proliferation[18]. LACTB is widely expressed in different mammalian tissues, most notably in the skeletal muscle, heart, and liver, and was found to negatively affect the proliferation of a variety of tumor cells *in vivo*, while it exerts little or no effect on growth of non-tumorigenic cells[18,25]. Moreover, mammalian LACTB promotes membrane organization[23], regulates mitochondrial respiratory complex I activity[26], and participates in cellular metabolic processes[27–29]. Given its strong relation to metabolic pathways, *LACTB* is also validated as an obesity gene capable of modifying adiposity[28].

LACTB is a conserved mitochondrial protein present in all vertebrates[30]. Amino acid sequence analyses show that serine protease LACTB shares sequence similarity to the penicillin binding protein and β-lactamases (PBP-βLs) family involved in peptidoglycan synthesis[30]. Given that the sequences of β-lactamases are conserved from bacteria to humans, it has been predicted that the molecular mechanisms underlying the cellular function are conserved for β-lactamases across species[30]. However, very little is known about the structural properties and function of LACTB in eukaryotic organisms. In contrast to its prokaryotic homologs, the human LACTB is expressed as a single polypeptide with an N-terminal mitochondrial targeting sequence[24,25]. Furthermore, mammalian LACTB dynamically assembles into filamentous polymers extending more than a hundred nanometers[23]. Filamentation has been observed for a variety of metabolic enzymes and is recognized as a general mechanism for regulating activity[31–38]. For LACTB, the mechanisms by which filament formation modulates enzyme activity remains unclear. Filaments of mammalian LACTB are reported to have a possible structural function in the spatial organization of mitochondrial IMS[23]. Recently, endurance exercise training has been shown to affect the polymerization of LACTB molecules in mice mitochondria suggesting that polymer assembly may have been directly influenced by metabolic activity in cells[29]. The formation of filaments may serve a regulatory function that results in more rapid activation or inhibition of the enzyme in response to changing cellular conditions.

A structure of a LACTB filament can help elucidate the biochemical characteristics of LACTB and permit a comprehensive mapping of polymerization interfaces. Here, we describe the atomic-resolution structure of the LACTB filament determined by using cryoEM. The structure reveals the inter-subunit interactions and overall assembly mechanism of LACTB. Furthermore, we provide supporting biochemical analysis of the assembly, where structure-guided mutations at different filament-forming interfaces unveil that polymerization is essential for the catalytic activity of

LACTB. Importantly, our work reveals that LACTB exerts its regulatory role by directly interacting with lipid membranes, building a basis for understanding the mechanism of mitochondrial membrane organization. These insights expand our understanding of human LACTB function and lay the foundation for further studies of its dynamic regulation and role in tumor suppression and metabolism.

RESULTS

Functional characterization of human LACTB filaments. To examine the molecular architecture of human LACTB, we purified near full-length LACTB (residues 97-547) lacking the N-terminal targeting sequence (Fig. 1a-c). The protein was fractionated further with Superose 6 Increase size-exclusion chromatography (SEC), wherein a single peak corresponding to a large molecule was observed on the elution profile indicating the formation of high-molecular-weight species (Fig. 1d). These oligomers seemed to be dynamic, as illustrated by the asymmetric and tailing peak on the gel filtration column (Fig. 1d). Analysis of the chromatogram peak using negative-stain electron microscopy (EM) revealed that LACTB assembled into filaments of several hundred nanometers in size (Fig. 1e). Our initial observations suggested that the polymers consisted of repeating LACTB subunits, resulting in flexible filaments with an outer radius of 150 Å and a wide range of length distribution (Fig. 1e). To test the proteolytic activity of LACTB filaments, we performed an *in vitro* substrate assay with the fluorogenic Ac-YVAD-AMC peptide and readily detected the enzymatic activity of purified wild-type (WT) LACTB in polymerized state (Fig. 1f). These results confirm that, like the other metabolic enzymes that self-assemble into filaments to organize and regulate metabolism[31,35,36,38], LACTB subunits can also form catalytically active filaments in solution.

LACTB assembles into a helical filament. To establish the structural basis for the LACTB filament assembly, we used cryoEM analysis. Initial cryoEM micrographs presented substantial challenges with respect to filament flexibility and clustering under cryogenic conditions. Sample preparation was subsequently optimized by adding detergent for cryoEM grid preparation. The two-dimensional (2D) classifications of overlapping filament segments and initial three-dimensional (3D) reconstructions encompassing multiple protomers revealed the helical architecture of the filament (Supplementary Fig. 1). After excluding low-quality segments, focus

classification and refinement of the central region was carried out with 58% of segments, which reduced heterogeneity and improved map quality (Supplementary Fig. 2). A final cryoEM reconstruction of the LACTB filament was obtained at an overall resolution of 3.1 Å with an imposed helical symmetry (Supplementary Fig. 2 and Table 1). A map with no noticeable differences (3.1 Å) was obtained when the final subset of segments was refined without imposing helical symmetry indicating that the helical assembly is highly symmetric (Supplementary Fig. 3). The resulting map quality was sufficient for unambiguous assignment of individual subunits, and to build an atomic model of the complete structure of the LACTB filament (Fig. 2 and Table 1). Except for the flexible loop region of the LACTB (residues 243 to 290), which extends to the solvent, all secondary structural elements and most side chain densities were clearly resolved in the cryoEM map (Fig. 2). The flexible loop (L6) may be weakly resolved due to conformational changes between protomers or because it is mostly disordered thus cannot be modeled. Further analysis of the structural data revealed that the basic building blocks of LACTB are dimers, which are stacked on each other and assembled into filaments with a helical twist of 48.25° and a rise of 21.63 Å (Fig. 2a).

Molecular architecture of human LACTB. LACTB has a globular structure with approximate dimensions of 60 Å X 55 Å X 45 Å and consist of a five-stranded β-sheet core (β1, β2, β7, β8, and β9) surrounded by two short two-stranded antiparallel β-sheets (β3 - β4 and β5 - β6) and ten α-helices (α1 - α10) (Fig. 2c-d). The β-sheet core is flanked by two helices (α1 - α10 and α2 - α8) on either side, creating a compact structure that forms the catalytic core (Fig. 2c). These α-helices and the β-sheet core are primarily stabilized by a network of hydrophobic interactions. While the α1 and α10 helices are connected to the β-sheet core with short loops, a 21-residue loop (L3) spans across the β-sheet core to link β2 to α2, and another long loop (L11) resides between the

β4 strand and the α8 helix (Fig. 2c-d). The α-helices, α3-α7 and α9, do not directly interact with the β-sheet core and form the outer surface of the filamentous assembly (Fig. 2c). Many charge-charge interactions stabilize the α-helices and the long loops of LACTB. Consistent with these observations, a Dali server search identified several prokaryotic and archaeal PBP-βL family of enzymes, such as ClbP (PDB ID: 4GDN), Pab87 peptidase (PDB ID: 2QMI), Penicillin-binding protein (pink, PDB ID: 3TG9), and D-amino-acid amidase (PDB ID: 2EFU), as close structural homologs of LACTB (Supplementary Fig. 4). While the resemblance in the overall fold of LACTB to prokaryotic homologs suggests the conservation of the enzymatic core, significant differences are observed in the loops and α-helices that surround the core structure (Supplementary Fig. 4a-d). Most importantly, the LACTB monomer includes a long L15 loop (residues 467 to 482) formed between β6 and β7 strands, a helix α4 (residues 227 to 242) that extends in parallel with the β-sheet core, and the predicted flexible loop (residues 243 to 290), all of which are not observed in other PBP-βLs proteins (Supplementary Fig. 4). Our 3.1 Å map also enabled the identification of the amino acid motifs (^{164}SISK^{167}, ^{323}YST^{325}, and ^{485}HTG^{487}) that contribute to the formation of the catalytic site, including the catalytic S164 residue, which are conserved across metazoan species (Supplementary Fig. 5a-c). The structure highlights a clearly defined cavity, which has a predominantly positively charged character (Supplementary Fig. 5b). The LACTB binding pocket is a ~20 Å deep cavity with a wider outer diameter (~20 Å) and a narrower inner diameter (~10 Å) near the catalytic site (Supplementary Fig. 5). In addition to the conserved active site residues, a number of positively charged (H216, H222 and K394) and aromatic residues (Y223, W454 and Y460) are in close proximity to the catalytic site (Supplementary Fig. 5). This suggests that LACTB substrates largely dock through charge-charge interactions, with a few polar residues responsible for the catalytic activity.

LACTB dimer interface governs filament assembly. We next sought to establish the mechanism of filament-assembly. The LACTB filaments assemble as stacked antiparallel dimers, where the buried surface area between the two protomers (A and B) is ~945 Å^2 (Fig. 3a). The structure shows that the antiparallel arrangement between two LACTB monomers results in symmetric interactions between two main dimer interfaces located on the L3 and L9 loops (Fig. 3a). Assembly of the LACTB dimer is mediated by the combined effects of sixteen hydrogen bond interactions between E149, N150, N364, E365, P366, I368, N370, R371, N385, and T386 residues, and two inter-molecular salt bridges between E149 and R371 (Fig. 3b). Conservation of these residues across mammalian species suggests that they may play an important role in subunit interactions (Supplementary Fig. 5c). Consistently, mutations targeting the dimer interface, including E149R-N150A double mutant and I368A-N370A-R371E triple mutant completely abolished the dimerization propensity as well as the filament formation of LACTB and produced a peak appearing at a lower molecular weight corresponding to a monomer in SEC analysis (Fig. 3c). Additionally, SDS-PAGE analysis and negative-stain electron micrographs of the peak fractions further confirmed our observations on the sizing column and showed that these substitutions remarkably destabilize the local complementary interactions and thus hamper the filament formation (Fig. 3c). On the other hand, mutation of N364A-E365A only modestly affected the overall filament stability and showed a gel filtration profile similar to the WT (Fig. 3c). Because the N364A-E365A double mutant did not completely hinder filament formation, we predicted that the dimer interface is likely stabilized by multiple polar and electrostatic interactions. To understand how filament assembly and disassembly influence the catalytic activity of LACTB, we characterized the activity of dimerization mutants in substrate assays. Compared to the WT LACTB, the dimer interface mutants, E149R-N150A and I368A-N370A-R371E, were completely inactive, while the N364A-E365A mutation only led to 20% reduction in LACTB activity (Fig. 3d). The negative effect of every dimer interface mutation disrupting the filament assembly suggests

that dimerization and subsequent polymerization is necessary to achieve maximal catalytic efficiency. These data provide a mechanism by which the strong interactions between the opposing dimer interface loops promote filament growth and result in increased enzyme activity by stabilizing the active architecture of the catalytic site. Taken together, we can confirm that the LACTB homodimers are the basic building blocks of the filaments and polymerization is strongly correlated with optimal enzyme activity.

LACTB filament elongation is mediated by multiple polymerization interfaces between subunits. When we evaluated multiple LACTB homologs, we decided to focus our structural analysis on the unique polymerization mechanism that brings the LACTB homodimers together to form the full filament. Polymerization is mediated by association between two LACTB homodimers (protomers A-B and C-D), where 48.25° helical rotation between stacked homodimers is necessary for growing a filament at either end (Fig. 4a). The inspection of the inter-dimer interface shows that three assembly contacts between neighboring subunits (A and C, A and D, and B and D) bridge antiparallel LACTB homodimers and drive filament assembly (Fig. 4a). The first polymer interface, which spans a buried solvent-accessible surface area of ~780 $Å^2$, is formed between the α1 helix and L3 along with the protruding L10 loop between β3 and β4 strands of protomers A and D (Fig. 4a-b). The two-fold symmetric interactions between protomers A and D from neighboring homodimers result in identical electrostatic surface potentials on both sides of the inter-dimer interface (Fig. 4a-b). Major contacts of this interface include several non-covalent interactions between residues D113, R117, E121, V122, R151, Y377, R382, L383, and S527, and a pair of symmetrical salt bridges between D113, D120 and R151 (Fig. 4a-b). To verify the functional relevance of these interactions for polymerization and catalytic activity, we performed mutagenesis studies on residues R117, R151, and Y377. Both R117E and R151E

charge-reversal mutations hindered the ability of LACTB to assemble into stable elongated filaments and yielded shorter assemblies containing a few LACTB protomers (Fig. 4d). Notably, the R151 salt bridge mutation reduced the proteolytic activity of LACTB by ~60% in substrate assays, whereas the R117E mutation only mildly affected the enzyme activity (Fig. 4e). Moreover, mutation of the conserved contact site residue Y377 to a lysine did not show major changes in filament length and formation compared to the WT but resulted in a greater effect (~70% reduction) regulating protease activity (Fig. 4d-e). These characteristics, together with the disruptive effect of charge-reversal mutations, indicate that complementary electrostatic forces stabilize the interactions between stacked LACTB dimers during filament formation.

The filament structure also shows a second polymer interface that has symmetric contact sites between protomers A and C and B and D, which bury ~540 $Å^2$ of solvent-accessible surface area (Fig. 4a). These two interfaces formed by the same residues and the interactions are mainly mediated by the charge complementarity and salt bridges (Fig. 4a-c). In our filament structure, the unique L15 loop that extends between β6 and β7 strands are embedded within the large pocket formed by α7 and α8 helices and L12 loop of the adjacent LACTB protomer (Fig. 4a-c). The most intimate contacts occur between L15 loop residues Y473, G474, S475, C476, and R477, and the conserved residues H352, D353, D355, Y369, A413, Y416, P432, and Y434 that line the surface of the pocket (Fig. 4c). Additional inter-molecular salt bridges are formed between H352 and E457, and D355 and R477, which stabilize the filament formation (Fig. 4c). To assess the importance of these interfaces, we produced a LACTB construct in which the L15 loop (V467 to Y482) is replaced by a glycine-glycine-serine (GGS) linker to disrupt the helical assembly interface. This mutant impaired the ability of LACTB to form long filaments, as judged using size-exclusion chromatography and negative-stain EM (Fig. 4d). We then tested this construct in substrate assays to measure catalytic activity. Not surprisingly, removal of the L15 loop completely abolished the enzymatic activity of the purified LACTB oligomers (Fig. 4e). Mutations

of individual L15 loop residues also hindered the enzymatic activity of LACTB. Substitution of residue G474 with tyrosine markedly reduced the catalytic activity of LACTB by ~85%, whereas charge-reversal mutation of R477 residue resulted in abrogation of catalytic function *in vitro* (Fig. 4e). We also characterized the role of the inter-molecular charge-charge interactions at the interface. Mutations targeting interface salt bridges, including H352A and D355K, did not affect the filament formation but decreased the enzymatic activity of LACTB by ~60% to 80%, respectively (Fig. 4d-e). Although these interface residues do not appear to participate in catalytic site formation as they are distant from the active site, they facilitate inter-subunit interactions that increase the stability and catalytic activity of the filament. Interestingly, structural comparison of human and prokaryotic PBP-βL family of enzymes unveiled that the LACTB structure is distinguished from its prokaryotic homologs by the addition of the 14-residue L15 loop, which is involved in filament assembly (Supplementary Fig. 4a-d). Moreover, multiple sequence alignment of the human LACTB and PBP-βL family of enzymes demonstrated very little sequence similarity for amino acids forming the L15 loop (Supplementary Fig. 4e). Consistent with our functional analysis, the L15 loop emerges as a regulatory element that controls not only the polymerization but also the catalytic activity of LACTB. Altogether, these results demonstrate that assembly of the filament and the L15 loop are required for catalytic activation of LACTB.

We next tested the possibility that changes in reactive oxygen species (ROS) in the mitochondrial IMS may influence the assembly of LACTB filaments. Mitochondrial ROS regulate a wide variety of cellular processes and are linked to multiple pathologies[39,40]. It was previously shown that hydrogen peroxide (H_2O_2) can disarrange actin polymers to provoke cell death during inflammation[41]. To investigate the impact of mitochondrial ROS on LACTB, we exposed protein samples to varying concentrations of H_2O_2 (0.01% to 1%) and showed that LACTB samples oxidized with H_2O_2 migrate more slowly than the native protein as deduced by SDS-PAGE analysis (Supplementary Fig. 6a). Such changes were consistent with the increase in H_2O_2

concentration. Subsequently, negative-stain EM imaging of protein samples revealed that oxidation at higher H_2O_2 concentrations hinder the filament formation of LACTB (Supplementary Fig. 6b). These data suggest that the H_2O_2-mediated oxidation of the protein could alter LACTB self-assembly dynamics and inhibit polymerization *in vitro*.

Mechanism of LACTB membrane organization. LACTB has been shown to localize to the mitochondrial IMS, where it assembles into polymers to regulate lipid metabolism[18,24]. Previous studies have also suggested a role for LACTB in mitochondrial membrane organization and micro-compartmentalization[23]. The structure of the LACTB filament can inform its mechanism of action and interactions with lipid membranes. To investigate whether there is a link between mitochondrial membrane organization and LACTB filament formation, we reconstituted freshly purified LACTB with liposomes that closely mimic the lipid composition of mitochondrial inner membranes in a buffer of physiological ionic strength and visualized binding *in vitro*. When analyzed by negative-stain EM, we directly observed the interplay between LACTB and lipid membranes (Fig. 5). LACTB filaments exhibited well-ordered, tightly packed conformation, and appeared to interact with liposomes via the tip of the polymer (Fig. 5a). These filaments were often tethered to two different liposomes on opposite ends forming a bridge between the two lipid membranes (Fig. 5b-e). Intriguingly, we also identified filaments that interact with liposomes from the side, where multiple protomers form intimate interactions with lipid membranes on either side (Fig. 5c-d). This second binding mode allows LACTB filaments to accommodate different membrane topologies and tightly associate with surrounding membranes, which enables membrane organization. These observations complement data that were previously obtained *in situ*[23], indicating that recombinant LACTB generates biologically relevant assemblies and binds membranes *in vitro* (Fig. 5). We postulate that the flexible loop region between residues 243-290 could facilitate membrane binding. Specifically, the human LACTB sequence contains a charged

and hydrophobic motif (^{259}KNxFxKFK^{266}) as well as a cluster of six basic side chains (^{274}KxRxxKxxKKK^{284}) with a remarkably electropositive character within this region that may form interactions with CL-containing liposomes *in vitro* (Supplementary Fig. 5c). However, these residues were not resolved in the structure due to the lack of EM density. While previous studies claim that this loop may promote self-assembly of the LACTB polymer through a coiled-coil segment[23], we propose that the flexible loop on the fully solvent-exposed exterior of the filament may adopt multiple conformations to accommodate different topologies and curvatures of opposing lipid membranes, thereby mediating protein-lipid interactions that would facilitate membrane organization. Consistent with this, the flexible loop is not conserved amongst prokaryotic and archaeal PBP-βL family of enzymes, which are not associated with lipid membranes[30], providing additional support for the relevance of this region for membrane binding (Supplementary Fig. 4e).

Molecular interpretation of disease-associated mutations. Given that human LACTB exerts tumor suppression activity in multiple carcinogenic cell lines, we next investigated cancer-specific missense mutations localized within LACTB. We classified LACTB disease mutations in terms of their localization to subunit-subunit interfaces and characterized their effect on the catalytic activity (Supplementary Fig. 7). Currently, over 200 *LACTB* gene variants have been identified, of which ~30% is considered pathogenic[42,43]. About 30% of the pathogenic variants cause frameshifts and premature truncation of the open reading frame, whereas the remaining ~70% are missense mutations that are linked to various cancers[42,43]. Mapping of disease-causing mutations onto our structure of human LACTB demonstrated that some of the pathogenic variants are clustered at the oligomerization interfaces, possibly culminating in a negative effect on filament assembly (Supplementary Fig. 7 and Supplementary Table 1). A number of mutations related to various types of cancers cluster at the LACTB dimer interface, including V148F, E149Q,

E363K, A372T, R371K, K380N, and R382C variants (Supplementary Fig. 7b). Our biochemical characterizations showed that the E149R and R371E charge-reversal mutations resulted in a profound multimerization defect and hindered the catalytic activity of human LACTB (Fig. 3c-d). Of note, V148, E149, and R371 belong to the L3 loop at the dimerization interface, where E149 and R371 forms hydrogen bonds and an inter-molecular salt bridge to stabilize the dimer (Fig. 3b and Supplementary Fig. 7b). Moreover, other variants such as R151S, D457K R469K, T472K, R480L, and Y482H, which are located at the polymer filament-forming interfaces, have also been associated with clinical anomalies (Supplementary Fig. 7). As described earlier, we analyzed the assembly properties of the LACTB R151E mutant *in vitro* and found that this mutant depressed the multimerization of human LACTB (Fig. 4d-f). Notably, we showed that the disruption of R151-D113 or H352-D457 electrostatic interactions results in ~60% reduction in the catalytic activity of human LACTB (Fig. 4d-e). We observed similar results when we assessed the functional role of protruding L15 loop (residues 467 to 482), which contains several disease-associated residues that are critical for filament formation and membrane organization activity of LACTB (Fig. 4d-e). Overall, mutations in these newly evident interfaces would likely have an impact on LACTB polymerization and catalytic activity and this provides important structural context as pathogenic variants in these interfaces are linked to several cancers.

DISCUSSION

Here, we investigated the molecular mechanism of the LACTB serine beta-lactamase, whose key functions in mitochondria include the regulation of metabolic pathways and tumor suppression by modulating mitochondrial lipid metabolism. Our high-resolution structure of the human LACTB filament shows that the enzyme forms a high-order helical filament, which is critical for its cellular function. These results offer new mechanistic insights into how LACTB assembles into filaments to control mitochondrial morphology as well as the efficiency of metabolic processes.

The basic building block of the helical structure consists of an antiparallel LACTB dimer. This unit then interacts with neighboring homodimers via charge-charge and polar interactions, which results in helical stacking of LACTB dimers and elongation of filaments (Fig. 6). We show that human LACTB contains novel structural features that are critical for polymerization. Although the active site motifs are conserved between LACTB and prokaryotic PBP-βL family of enzymes, phylogenetic and structural analyses demonstrate that the residues involved in polymerization are only conserved in higher eukaryotes, suggesting that LACTB has evolved from its prokaryotic counterparts to fulfill different physiological functions in mammals (Supplementary Fig. 5). It is intriguing that LACTB requires unique contacts to robustly polymerize into filaments and to enable catalytic activity. While the benefits of polymeric enzymes are not fully understood, there are several theories of filamentous enzymes exhibiting kinetic advantages. One such kinetic model involves rapid activation of enzymes through filament formation[44–47]. For instance, the bacterial SgrIR protein, which is a filament forming restriction endonuclease, polymerizes rapidly at either end of the filament to stimulate enzyme activity and increase DNA-binding specificity[48,49]. Similarly, many metabolic enzymes such as cytidine triphosphate synthase (CTPS) and inosine monophosphate dehydrogenase (IMPDH) form filaments in bacteria and eukaryotes to modulate enzyme activity[31–34]. Interestingly, CTP-induced polymerization of bacterial CTPS results in

decreased catalytic activity, whereas substrate-bound human CTPS filaments display increased enzymatic activity, suggesting that filament formation can tune the activity of metabolic enzymes differently in response to distinct metabolic cues in different species[31]. Additionally, an isoform of human acetyl-CoA carboxylase in the mitochondria forms active and inactive helical filaments through allosteric regulation by citrate and the binding of BRCA1, respectively, revealing a unique form of enzyme regulation via large scale conformational changes in filament architecture[35]. The structure of the LACTB filament, together with extensive mutagenesis studies, show that polymerization is essential for the catalytic activity of the enzyme (Fig. 3). However, the polymerization interfaces do not participate in active site formation (Fig. 4). A possible explanation for this increased enzymatic activity upon filament assembly is that the binding of LACTB protomers indirectly stabilizes the regions involved in substrate binding and thus enhances the catalytic activity of LACTB. The stabilization of the LACTB filament through multiple intra- and inter-dimeric interfaces that are largely mediated by charged and polar interactions strongly suggest that the filament assembly is responsible for the observed amplification of LACTB activity in our biochemical data. Our results suggest that the catalytic activity of human LACTB is allosterically regulated by stabilizing an intrinsically inactive state upon filament formation, independent of substrate binding, thus holding the enzyme in an active conformation. Filamentation appears to be an evolutionarily conserved mechanism in a diverse array of biochemical and biological pathways in cells and provide an added layer of regulation in the form of rapid activation or inhibition[46,50]. By characterizing distinct interactions in LACTB filaments our data provide structural basis for manipulating LACTB polymerization in vivo.

Many different enzymes dynamically form filaments in response to changing physiological conditions in cells[31,34,35,37,51]. In addition to modulating enzyme activity through polymerization, an unexpected feature of the LACTB filaments is their ability to interact with lipid membranes.

Filamentation of human LACTB is important for the spatial organization of mitochondrial membranes[23]. However, it is not clear whether the catalytic activity of LACTB plays a role in membrane organization in mitochondria as its direct substrate remains unknown. Unlike many membrane-associated proteins such as conserved septin proteins in mammals[52], membrane binding does not influence LACTB polymerization through end-to-end association of the homodimers. It is striking that while many regulatory enzymes polymerize to allosterically tune enzyme kinetics[46], LACTB exerts a dual function and forms exclusively cooperative filaments to interact with mitochondrial membranes from the inside. We showed that the LACTB filaments are unique as they contain specific sequences to interact directly with membranes (Fig. 5). Although the physiological significance of our in vitro observations remains to be fully elucidated, we anticipate further roles in mitochondrial morphogenesis and in processes, where strong membrane association is needed. Mitochondrial membranes have a unique lipid composition that is important for organelle's morphology and proper function of membrane-associated processes[7]. In addition to the major phospholipids PE and PC, which account for a large portion of mitochondrial membrane lipids, mitochondria-exclusive phospholipid cardiolipin (CL) is a distinguishing component of the mitochondrial IM that is known to participate in a wide range of mitochondrial processes[10]. CL directly interacts with positively charged surfaces of numerous mitochondrial proteins with its negatively charged headgroup and contributes to the dynamic membrane organization in mitochondria[53,54]. Negative-stain EM imaging revealed that LACTB filaments have a high affinity for cardiolipin-containing lipid bilayers and manifest two different membrane binding modes (Fig. 5). We postulate that LACTB filaments are recruited to the inner/outer membrane by electrostatic interactions between negatively charged phospholipids and the flexible polybasic surface loop of LACTB. When the tip of the LACTB filaments binds lipid membranes, subunits of adjacent homodimers form additional protein-lipid interactions through lateral associations, increasing the filament contacts with the membrane surface. Furthermore,

subunits on the opposite end of the filament binds membranes in a similar fashion and engage in lateral associations via interactions of several subunits, thus bringing the two membranes into close apposition. We therefore propose that upon forming filaments between the two membranes, human LACTB can act like a molecular zipper and regulate mitochondrial membrane organization by controlling the distance between the two membranes. LACTB filaments display a strong driving force for spatial arrangement of membranes, thus providing a structural foundation for a wide variety of normal and pathological processes.

Overexpression of LACTB positively contributes to the apoptosis and suppression of tumor cells *in vivo*[18]. However, it has been reported that LACTB expression has been significantly downregulated by promoter methylation, histone deacetylation, and several microRNAs (miRNAs) in various cancers, including in breast cancers, uterine cancer, colorectal cancers, gliomas, melanomas, hepatocellular carcinomas, and oxaliplatin-resistant gastric cancer[19–22,55–58]. The downregulation of LACTB expression is often correlated with a poor prognosis in these anomalies[55,58]. Dysregulation of LACTB is also associated with obesity and atherosclerosis potentially due to its involvement in metabolic pathways, in particular the phospholipid metabolism in mitochondria[18,27,28]. The process of polymerization requires a critical concentration of monomeric protein for filament formation, where larger self-assemblies can be formed as a result of protein crowding[46]. Our results indicate that both LACTB-mediated mitochondrial membrane organization and regulation of lipid metabolism may be directly linked to its ability to form higher-order assemblies. For instance, a possible mechanism for the regulation of PISD by LACTB may involve the formation of micron-scale filaments that control the distance between the inner and outer mitochondrial membranes such that the reaction to form PE by PISD1 is unable to occur due to spatial rearrangement[59]. The downregulation of LACTB mRNA and protein levels by cellular factors would result in reduced protein quantities in mitochondria, hinder filament

formation, limit the length of self-assembled filaments, and decrease the catalytic activity of the enzyme *in vivo*; therefore, debilitate its regulatory role in lipid metabolism. Since PE plays an important role in promoting mitochondrial dynamics[14,60,61], the dysregulation of PE homeostasis due to a disruption to LACTB self-assembly mechanism would be detrimental for mitochondrial function spatial organization. However, the exact mechanism underlying LACTB on tumor suppression, the association between downregulation of LACTB gene expression by miRNAs, and the effect on filament formation have yet to be determined.

Finally, our ability to map mutations that are identified in various cancers to the LACTB structure expands the breadth of deficiency mechanisms (beyond downregulation of LACTB by several miRNAs) to additionally include the impaired ability of LACTB to correctly assemble into a filament. Our structural model encompasses nearly all human cancer-associated missense mutations in LACTB and lays the foundation for characterizing additional mechanisms leading to LACTB perturbation in the regulation of lipid metabolism and mitochondrial membrane organization. This study uncovers an important aspect to how LACTB functions as a tumor suppressor and provides a foundation for future cancer research and drug therapy with LACTB as a target.

METHODS

Protein expression and purification

The gene encoding human LACTB (residues 1-547) was obtained from DNASU (HsCD00629745). The DNA sequence for human LACTB (residues 97-547) was subcloned into the multiple cloning site of pCA528 bacterial expression vector. LACTB was tagged with an N-terminal 6x-His tag followed by a SUMO tag. All mutant constructs were generated by a two-step site-directed mutagenesis PCR protocol. The plasmid was transformed into *Escherichia coli* BL21(DE3)-RIPL cells and expressed in ZYP-5052 auto-induction media at 18°C for 16 h when OD_{600} reached 0.6-0.8. Cells were harvested with centrifugation (Sorvall RC-5B Superspeed Centrifuge) at 10,800 rpm (39,531x *g*) for 20 min at 4 °C. The supernatant was then discarded, and the cell pellets were resuspended in lysis buffer (50 mM HEPES-NaOH, pH 7.5, 500 mM NaCl, 5 mM $MgCl_2$, 20 mM imidazole, 1mM CHAPS (Anatrace), 5mM 2-mercaptoethanol, 10% (v/v) glycerol) supplemented with 0.5% (v/v) Triton X-100, 0.5 mg DNase I, and 1X EDTA-free complete protease inhibitor cocktail (Roche). The cells were lysed with an Emusliflex C3 Homogenizer and the cell lysate was clarified by centrifugation (Sorvall RC-5B Superspeed Centrifuge) at 15,000 rpm (68,040x *g*) at 4 °C for 45 min. The supernatant was incubated with Ni-NTA agarose beads (Qiagen) for 1 h. The Ni-NTA beads were washed with 20 column volumes (CV) of lysis buffer, 10 CV of wash buffer (50 mM HEPES-NaOH, pH 7.5, 1M NaCl, 5 mM $MgCl_2$, 20 mM imidazole, 1mM CHAPS, 5mM 2-mercaptoethanol, 10% (v/v) glycerol), and 10 CV of lysis buffer again before the protein was eluted with 5 CV elution buffer (50 mM HEPES-NaOH, pH 7.5, 500 mM NaCl, 5 mM $MgCl_2$, 500 mM imidazole, 1mM CHAPS and 10% (v/v) glycerol). The sample was then dialyzed into lysis buffer containing Ulp1 protease to remove the N-terminal 6x-His-SUMO tag overnight at 4 °C. The dialyzed protein was concentrated using a 30 kDa MWCO concentrator (Millipore) and was further purified by size-exclusion chromatography on a Superose 6 Increase 10/300 GL column (Cytiva) equilibrated with purification buffer (20 mM HEPES-NaOH,

pH 7.5, 140 mM NaCl, 10 mM KCl, 1mM $MgCl_2$, and 1 mM DTT). A typical size-exclusion profile for WT LACTB consisted of a large peak containing LACTB filaments eluting within the void volume (V_0) of the column. Fractions of LACTB were analyzed by SDS-PAGE. Freshly purified samples were used for cryoEM grid preparation and *in vitro* substrate binding assays.

Negative-stain electron microscopy

The LACTB assembly was purified as described above. Size-exclusion peak fractions corresponding to LACTB were diluted to ~2.0 µM for negative-stain transmission electron microscope (TEM). Samples were prepared by applying 4 µl of purified LACTB applied onto glow-discharged carbon-coated copper grids (400 mesh), and negatively stained with 0.75% (w/v) uranyl formate (UF) following an established protocol[62]. Briefly, the samples were incubated on the grid for 1 min and then blotted off with a filter paper. Subsequently, samples on grids were stained with UF for 45 s and air dried for 2 min at room temperature. The grids were imaged using a Tecnai T12 Spirit LaB6 filament TEM (FEI) equipped with an AMT 2k x 2k side-mounted CCD camera and operated at a voltage of 100 kV. The micrographs were collected at a nominal magnification of 120,000x at the specimen level with a calibrated pixel size of 5.28 Å per pixel.

CryoEM sample preparation and data acquisition

Prior to cryoEM grid preparation, an aliquot of purified LACTB was buffer exchanged to a freezing buffer (20 mM HEPES-NaOH, pH 7.5, 140 mM NaCl, 10 mM KCl, 1 mM $MgCl_2$, 1mM DTT, 1% glycerol, and 1 mM CHAPS) by centrifugation at 1000x *g* for 2 minutes with a micro-spin desalting column (Thermo Scientific Zeba) at 4 °C. Aliquots of 4 µl of protein samples (0.3 mg ml^{-1} or ~6 µM) were applied to glow-discharged R1.2/1.3 200 Cu mesh grids (Quantifoil). After 30 s, the grids were blotted for 3 seconds and plunged into liquid ethane using a Leica EM GP2 Automatic Plunge Freezer operated at 10 °C and 90% humidity. Micrographs were acquired using a Titan

Krios TEM (FEI) operated at 300 kV and equipped with a K3 Summit direct electron detector (Gatan). Images of frozen-hydrated filaments of LACTB were collected in counting mode at a nominal magnification of 29,000x corresponding to an image pixel size of 0.8211 Å on the specimen level, applying a defocus range of with a -0.5 to -1.5 µm. A total of 7643 dose-fractionated movies were recorded with the SerialEM software[63] multishot method over nine neighboring holes (3 x 3). The dose rate was 1.05 electrons/Å^2/frame, with a frame rate of 0.07 s, resulting in a total exposure time of 3.985 s and a total accumulated dose of 59.58 electrons per Å^2 (57 frames). CryoEM data collection parameters are summarized in Table 1.

Image analysis and 3D reconstruction

The alignment and dose-weighted summation of raw movie stacks were carried out using MotionCor2[64]. Contrast transfer function (CTF) estimation were performed on aligned, non-dose-weighted micrographs using CTFFIND4[65]. All subsequent processing steps were performed using Relion 3.1[66,67]. A total of 34,636 filament coordinates were manually picked and filament segments with 90% overlap were extracted by using a box size of 320 pixels. All segments (430,592) were then subjected to multiple rounds of reference-free two-dimensional (2D) classification with 100 classes to identify structurally homogeneous subsets. After 2D classification, a featureless cylinder-shaped electron density map with a 160 nm diameter was generated in Relion and used as an initial reference for 3D auto-refinement with C1 symmetry. The resulting refined map showed clear secondary structure features and was used to estimate the helical parameters. Using this 4.3 Å reconstruction, an initial 3D classification was performed with C1 symmetry, and the segments from the best 3D classes (248,548 segments) were selected for high-resolution 3D auto-refinement. Subsequently, these segments were 3D auto-refined with a soft mask, central Z length of 45% of the box size (helical_z_percentage=0.45), and imposing starting helical parameters of 21.59 Å rise and 48.91° twist, yielding a 3D reconstruction with an overall resolution

of 3.7 Å. To improve this density map, the final particle segments were subjected to iterative rounds of focused 3D auto-refinement, CTF refinement, and Bayesian polishing to obtain a final 3D reconstruction of a right-handed helical assembly at 3.1 Å resolution. The helical parameters converged to a rise of 21.63 Å and a twist of 48.25° per subunit. A reconstruction without imposing symmetry was also generated at 3.1 Å resolution after focus refinement using a similar mask on the filament. The final reported resolutions are based on the gold-standard Fourier shell correlation (FSC) = 0.143 criterion. Maps were sharpened by applying a negative *B* factor as determined by the Relion post-processing program. The local resolution estimation was calculated by ResMap using half-map reconstructions[68].

Model building and refinement

Model building was carried out using the 3.1 Å cryoEM map of the human LACTB filament. The Alphafold[69] structure of monomeric LACTB was used as an initial model for atomic model building. The model was manually fitted into the cryoEM density map using UCSF Chimera[70] and then rigid body refined using the real-space refinement procedure implemented in the program PHENIX[71]. Atomic coordinates of the human LACTB (residues 97-547) filament were manually rebuilt using the program Coot[72] and the final models were iteratively refined against the cryoEM density map. The real space-refinement of models with global minimization, local grid search, secondary structure, and geometric restraints applied was performed using the software PHENIX[71]. Secondary structure elements and side chains for the majority of the residues were unambiguously resolved. Each residue was manually inspected, and correction of the refined coordinates was performed by applying torsion, planar peptide, and Ramachandran restraints during manual rebuilding in Coot[72].

Validation and structural analysis

The stereochemistry and geometry of the final model was evaluated by MolProbity[73]. CryoEM maps and atomic models were analyzed, and figures were generated using UCSF ChimeraX[74], UCSF Chimera[70], and PyMOL (The PyMOL Molecular Graphics System, Version 2.0 Schrödinger, LLC). Negative-stain EM images were analyzed using FIJI[75]. Surface potential renderings were generated using the APBS plugin in PyMOL[76]. Structural and chemical properties of macromolecular interfaces and surfaces were analyzed by the PISA server[77]. The fold conservation analysis was performed with Dali server[78] and structural comparisons to the PBP-βL family of enzymes and RMSD calculations were carried out using the CLICK server[79]. Sequence alignment of the LACTB homologs as well as the PBP-βL family of enzymes were generated using Clustal Omega[80] and sequence conservation figures were prepared by using the Clustal Omega alignment file and LACTB model in ESPript server 3.0[81]. Schematic diagrams were generated by using BioRender.com. The statistics of the cryoEM helical reconstruction and model refinement were summarized in Table 1.

LACTB *in vitro* substrate assay

To determine the catalytic activity of the wild-type and mutant LACTB, the cleavage of the fluorogenic Ac-YVAD-AMC peptide (Enzo Life Sciences) was measured at an excitation wavelength of 380 nm and an emission wavelength of 460 nm using a CLARIOstar microplate reader. All assays were performed at room temperature and the total reaction volumes were 20 µl. Briefly, 10 µl of purified LACTB protein was mixed with a reaction buffer containing 20 mM HEPES-NaOH, pH 7.5, 140 mM NaCl, 10 mM KCl, 1 mM $MgCl_2$, 1 mM DTT, and 0.01% NP-40 detergent (AmericanBio) to generate a final protein concentration of 15 nM. Reactions were initiated by adding 100 µM concentrations of the substrate Ac-YVAD-AMC (dissolved in DMSO and prediluted to 200 µM in reaction buffer) to the enzyme in a 384 well black polystyrene assay plate (Costar 3916). The reactions were run in three independent replicates for 1,200 s and

fluorescence was measured every 10 s. The raw data were averaged to determine reaction rates from the linear part of the curve and include standard deviation.

H_2O_2 treatment of LACTB filaments

An aliquot of purified LACTB was diluted to 0.15 mg ml^{-1}. Aliquots of 10 µl of the protein sample were incubated with 5 µl of varying concentrations of H_2O_2 for 30 minutes. The final concentrations were 0.01% H_2O_2 (v/v), 0.025%, 0.05%, 0.1%, 0.25%, 0.5%, 0.75%, and 1.0%. The final concentration of protein was 0.1 mg ml^{-1}. The samples were analyzed by SDS PAGE using a 4-15% precast gel (BioRad) at 100 V. The 0.1%, 0.5%, and 1.0% H_2O_2 (v/v) samples were stained on glow-discharged carbon-coated copper grids with UF as described above and visualized with a Tecnai T12 Spirit TEM (FEI) operated at a voltage of 100 kV. The micrographs were collected at a nominal magnification of 120,000x at the specimen level with a calibrated pixel size of 5.28 Å per pixel.

Preparation of lipid vesicles and LACTB membrane binding reactions

To determine the membrane binding activity of human LACTB, the lipid composition of mitochondrial inner membrane was used to prepare vesicles as described previously[82]. The lipid stock solutions were resuspended in chloroform, methanol and water mixture (20:9:1, (v/v/v)) and stored at -20°C. 1-palmitoyl-2-oleoyl-glycero-3-phosphocholine (POPC), 1-palmitoyl-2-oleoyl-sn-glycero-3-phosphoethanolamine (POPE), L-α-lysophosphatidylinositol (Soy Lyso PI), 1',3'-bis[1,2-dioleoyl-sn-glycero-3-phospho]-glycerol (cardiolipin $(18:1)_4$) (Avanti Polar Lipids) were mixed in a molar ratio of POPC:POPE:PI:CL; 45:22:8:25. The lipid mixture was then dried as a thin film in a glass tube under a gentle stream of nitrogen, and incubated in a vacuum desiccator for 4 h to remove excess solvent. Following dehydration, the lipid film was resuspended for 30 min at room temperature in a liposome buffer containing 20mM HEPES-NaOH, pH 7.5 and

150mM NaCl. The suspension was extruded through polycarbonate membranes with 50 nm pore diameter using Avanti Mini Extruder (Avanti Polar Lipids) to obtain unilamellar liposomes. 20 µl aliquots of rehydrated lipids were flash-frozen in liquid nitrogen and stored at -80°C.

For liposome binding assays, freshly purified 2 µM wild-type LACTB was incubated with 0.5 mg ml^{-1} unilamellar liposomes or the liposome reaction buffer (20 mM HEPES-NaOH, pH 7.5, 140 mM NaCl, 10 mM KCl, 1 mM $MgCl_2$, 1 mM DTT) for 4 h at room temperature. Subsequently, the reaction mixture was applied onto glow-discharged carbon-coated copper grids and negatively stained with UF. The membrane binding activity of LACTB filaments was assessed by negative-stain TEM. Images were collected using a Tecnai T12 Spirit TEM (FEI) equipped with an AMT 2k x 2k side-mounted CCD camera as described above.

Data Accessibility

All of the 3D cryoEM data that support the findings of this study have been deposited in Electron Microscopy Data Bank with the accession code: EMDB-26595. The model coordinates have been deposited in the Protein Data Bank under accession code PDB ID: 7ULW.

Acknowledgements

We thank the current members of the Aydin laboratory for helpful discussions and assistance on this project. We specially thank Charles Moe at the BioChemistry Krios Electron Microscopy (BioKEM) Facility of the University of Colorado Boulder for his support with data collection and EM infrastructure; Garry Morgan and Courtney Ozzello at the EM Services Core Facility of the University of Colorado Boulder for electron microscopy training and support; the Shared Instrument Pool (SIP) core facility (RRID: SCR_018986) of the Department of Biochemistry at the University of Colorado Boulder for the use of the shared research instrumentation infrastructure; Dr. Annette Erbse for assistance with biophysical instruments and support; Dr. Chris Ebmeier and the Mass Spectrometry Core Facility of the University of Colorado Boulder for mass spectrometry analysis; Dr. Kelly Du Pont for assistance with computer infrastructure. We also thank Professor Karolin Luger for her support and kindly sharing the equipment for the fluorescence-based activity assays. The results shown here are in part based upon data generated by the TCGA Research Network: https://www.cancer.gov/tcga.

Author contributions

J.A.B. and L.R.S. performed all the cloning, mutagenesis, biochemical and biophysical characterizations, negative-stain EM, cryoEM experiments, and analysis, determined the cryoEM structures, and conducted model building, refinement, and validation of the cryo-EM structures. J.R. performed the fluorescence-based activity assays and analyzed the results. A.P.V. carried out biochemical characterizations and negative-stain EM experiments. H.A. supervised the research. All authors analyzed the data, discussed the results, and wrote the manuscript.

Competing interests

The authors declare no competing interests.

Correspondence and requests for materials should be addressed to H.A.

REFERENCES

1. Mottis, A., Herzig, S. & Auwerx, J. Mitocellular communication: Shaping health and disease. *Science* **366**, 827–832 (2019).
2. Spinelli, J. B. & Haigis, M. C. The multifaceted contributions of mitochondria to cellular metabolism. *Nat. Cell Biol.* **20**, 745–754 (2018).
3. Iovine, J. C., Claypool, S. M. & Alder, N. N. Mitochondrial compartmentalization: emerging themes in structure and function. *Trends Biochem. Sci.* **46**, 902–917 (2021).
4. Friedman, J. R. & Nunnari, J. Mitochondrial form and function. *Nature* **505**, 335–343 (2014).
5. Chan, D. C. Mitochondrial Dynamics and Its Involvement in Disease. *Annu. Rev. Pathol. Mech. Dis.* **15**, 235–259 (2020).
6. Eisner, V., Picard, M. & Hajnóczky, G. Mitochondrial dynamics in adaptive and maladaptive cellular stress responses. *Nat. Cell Biol.* **20**, 755–765 (2018).
7. Mayr, J. A. Lipid metabolism in mitochondrial membranes. *J. Inherit. Metab. Dis.* **38**, 137–144 (2015).
8. Stefely, J. A. & Pagliarini, D. J. Biochemistry of Mitochondrial Coenzyme Q Biosynthesis. *Trends Biochem. Sci.* **42**, 824–843 (2017).
9. Manicki, M. *et al.* Structure and functionality of a multimeric human COQ7:COQ9 complex. 2021.11.15.468694 (2021) doi:10.1101/2021.11.15.468694.
10. Mårtensson, C. U., Doan, K. N. & Becker, T. Effects of lipids on mitochondrial functions. *Biochim. Biophys. Acta BBA - Mol. Cell Biol. Lipids* **1862**, 102–113 (2017).
11. Basu Ball, W., Neff, J. K. & Gohil, V. M. The role of nonbilayer phospholipids in mitochondrial structure and function. *FEBS Lett.* **592**, 1273–1290 (2018).
12. Steenbergen, R. *et al.* Disruption of the Phosphatidylserine Decarboxylase Gene in Mice Causes Embryonic Lethality and Mitochondrial Defects. *J. Biol. Chem.* **280**, 40032–40040 (2005).

13. Calzada, E. *et al.* Phosphatidylethanolamine made in the inner mitochondrial membrane is essential for yeast cytochrome bc1 complex function. *Nat. Commun.* **10**, 1432 (2019).
14. Tasseva, G. *et al.* Phosphatidylethanolamine Deficiency in Mammalian Mitochondria Impairs Oxidative Phosphorylation and Alters Mitochondrial Morphology. *J. Biol. Chem.* **288**, 4158–4173 (2013).
15. Snaebjornsson, M. T., Janaki-Raman, S. & Schulze, A. Greasing the Wheels of the Cancer Machine: The Role of Lipid Metabolism in Cancer. *Cell Metab.* **31**, 62–76 (2020).
16. Vyas, S., Zaganjor, E. & Haigis, M. C. Mitochondria and Cancer. *Cell* **166**, 555–566 (2016).
17. Porporato, P. E., Filigheddu, N., Pedro, J. M. B.-S., Kroemer, G. & Galluzzi, L. Mitochondrial metabolism and cancer. *Cell Res.* **28**, 265–280 (2018).
18. Keckesova, Z. *et al.* LACTB is a tumour suppressor that modulates lipid metabolism and cell state. *Nature* **543**, 681–686 (2017).
19. Ma, Y. *et al.* LACTB suppresses melanoma progression by attenuating PP1A and YAP interaction. *Cancer Lett.* **506**, 67–82 (2021).
20. Xu, W., Yu, M., Qin, J., Luo, Y. & Zhong, M. LACTB Regulates PIK3R3 to Promote Autophagy and Inhibit EMT and Proliferation Through the PI3K/AKT/mTOR Signaling Pathway in Colorectal Cancer. *Cancer Manag. Res.* **12**, 5181–5200 (2020).
21. Li, H.-T., Dong, D.-Y., Liu, Q., Xu, Y.-Q. & Chen, L. Overexpression of LACTB, a Mitochondrial Protein That Inhibits Proliferation and Invasion in Glioma Cells. *Oncol. Res. Featur. Preclin. Clin. Cancer Ther.* **27**, 423–429 (2019).
22. Zeng, K. *et al.* LACTB, a novel epigenetic silenced tumor suppressor, inhibits colorectal cancer progression by attenuating MDM2-mediated p53 ubiquitination and degradation. *Oncogene* **37**, 5534–5551 (2018).
23. Polianskyte, Z. *et al.* LACTB is a filament-forming protein localized in mitochondria. *Proc. Natl. Acad. Sci.* **106**, 18960–18965 (2009).

24. Hung, V. *et al.* Proteomic Mapping of the Human Mitochondrial Intermembrane Space in Live Cells via Ratiometric APEX Tagging. *Mol. Cell* **55**, 332–341 (2014).
25. Smith, T. S. *et al.* Identification, Genomic Organization, and mRNA Expression of LACTB, Encoding a Serine β-Lactamase-like Protein with an Amino-terminal Transmembrane Domain. *Genomics* **78**, 12–14 (2001).
26. Pagliarini, D. J. *et al.* A Mitochondrial Protein Compendium Elucidates Complex I Disease Biology. *Cell* **134**, 112–123 (2008).
27. Chen, Y. *et al.* Variations in DNA elucidate molecular networks that cause disease. *Nature* **452**, 429–435 (2008).
28. Yang, X. *et al.* Validation of candidate causal genes for obesity that affect shared metabolic pathways and networks. *Nat. Genet.* **41**, 415–423 (2009).
29. Gonzalez-Franquesa, A. *et al.* Mass-spectrometry-based proteomics reveals mitochondrial supercomplexome plasticity. *Cell Rep.* **35**, 109180 (2021).
30. Peitsaro, N. *et al.* Evolution of a family of metazoan active-site-serine enzymes from penicillin-binding proteins: a novel facet of the bacterial legacy. *BMC Evol. Biol.* **8**, 26 (2008).
31. Lynch, E. M. *et al.* Human CTP synthase filament structure reveals the active enzyme conformation. *Nat. Struct. Mol. Biol.* **24**, 507–514 (2017).
32. Lynch, E. M. & Kollman, J. M. Coupled structural transitions enable highly cooperative regulation of human CTPS2 filaments. *Nat. Struct. Mol. Biol.* **27**, 42–48 (2020).
33. Lynch, E. M. *et al.* Structural basis for isoform-specific inhibition of human CTPS1. *Proc. Natl. Acad. Sci.* **118**, e2107968118 (2021).
34. Johnson, M. C. & Kollman, J. M. Cryo-EM structures demonstrate human IMPDH2 filament assembly tunes allosteric regulation. *eLife* **9**, e53243 (2020).
35. Hunkeler, M. *et al.* Structural basis for regulation of human acetyl-CoA carboxylase. *Nature* **558**, 470–474 (2018).

36. Kim, G. *et al.* Aldehyde-alcohol dehydrogenase forms a high-order spirosome architecture critical for its activity. *Nat. Commun.* **10**, 4527 (2019).

37. Webb, B. A., Dosey, A. M., Wittmann, T., Kollman, J. M. & Barber, D. L. The glycolytic enzyme phosphofructokinase-1 assembles into filaments. *J. Cell Biol.* **216**, 2305–2313 (2017).

38. Petrovska, I. *et al.* Filament formation by metabolic enzymes is a specific adaptation to an advanced state of cellular starvation. *eLife* **3**, e02409 (2014).

39. Sena, L. A. & Chandel, N. S. Physiological Roles of Mitochondrial Reactive Oxygen Species. *Mol. Cell* **48**, 158–167 (2012).

40. Auten, R. L. & Davis, J. M. Oxygen Toxicity and Reactive Oxygen Species: The Devil Is in the Details. *Pediatr. Res.* **66**, 121–127 (2009).

41. DalleDonne, I., Milzani, A. & Colombo, R. H2O2-treated actin: assembly and polymer interactions with cross-linking proteins. *Biophys. J.* **69**, 2710–2719 (1995).

42. Karczewski, K. J. *et al.* The mutational constraint spectrum quantified from variation in 141,456 humans. *Nature* **581**, 434–443 (2020).

43. Tate, J. G. *et al.* COSMIC: the Catalogue Of Somatic Mutations In Cancer. *Nucleic Acids Res.* **47**, D941–D947 (2019).

44. Park, C. K. & Horton, N. C. Structures, functions, and mechanisms of filament forming enzymes: a renaissance of enzyme filamentation. *Biophys. Rev.* **11**, 927–994 (2019).

45. Lynch, E. M., Kollman, J. M. & Webb, B. A. Filament formation by metabolic enzymes—A new twist on regulation. *Curr. Opin. Cell Biol.* **66**, 28–33 (2020).

46. Aughey, G. N. & Liu, J.-L. Metabolic regulation via enzyme filamentation. *Crit. Rev. Biochem. Mol. Biol.* **51**, 282–293 (2016).

47. Simonet, J. C., Burrell, A. L., Kollman, J. M. & Peterson, J. R. Freedom of assembly: metabolic enzymes come together. *Mol. Biol. Cell* **31**, 1201–1205 (2020).

48. Polley, S., Lyumkis, D. & Horton, N. C. Mechanism of Filamentation-Induced Allosteric

Activation of the SgrAI Endonuclease. *Structure* **27**, 1497-1507.e3 (2019).

49. Barahona, C. J. *et al.* The Need for Speed: Run-On Oligomer Filament Formation Provides Maximum Speed with Maximum Sequestration of Activity. *J. Virol.* **93**, e01647-18 (2019).
50. Egelman, E. H. Actin's prokaryotic homologs. *Curr. Opin. Struct. Biol.* **13**, 244–248 (2003).
51. Burrell, A. L. *et al.* IMPDH1 retinal variants control filament architecture to tune allosteric regulation. *Nat. Struct. Mol. Biol.* **29**, 47–58 (2022).
52. Szuba, A. *et al.* Membrane binding controls ordered self-assembly of animal septins. *eLife* **10**, e63349 (2021).
53. Liang, K. *et al.* Cryo-EM structure of human mitochondrial trifunctional protein. *Proc. Natl. Acad. Sci.* **115**, 7039–7044 (2018).
54. Xia, C., Fu, Z., Battaile, K. P. & Kim, J.-J. P. Crystal structure of human mitochondrial trifunctional protein, a fatty acid β-oxidation metabolon. *Proc. Natl. Acad. Sci.* **116**, 6069–6074 (2019).
55. Zhang, J. *et al.* Upregulation of miR-374a promotes tumor metastasis and progression by downregulating LACTB and predicts unfavorable prognosis in breast cancer. *Cancer Med.* **7**, 3351–3362 (2018).
56. Yang, F. *et al.* LACTB induced apoptosis of oxaliplatin-resistant gastric cancer through regulating autophagy-mediated mitochondrial apoptosis pathway. 16.
57. Liu, J. *et al.* Targeted Nanotherapeutics Using LACTB Gene Therapy Against Melanoma. *Int. J. Nanomedicine* **16**, 7697–7709 (2021).
58. Xue, C. *et al.* Low expression of LACTB promotes tumor progression and predicts poor prognosis in hepatocellular carcinoma. Am. J. Transl. Res. **10**(12):4152-4162 (2018).
59. Eriksson, O., Lalowski, M. & Lindholm, D. Commentary: LACTB is a tumour suppressor that modulates lipid metabolism and cell state. *Front. Physiol.* **8**, 396 (2017).
60. Chan, E. Y. L. & McQuibban, G. A. Phosphatidylserine Decarboxylase 1 (Psd1) Promotes

Mitochondrial Fusion by Regulating the Biophysical Properties of the Mitochondrial Membrane and Alternative Topogenesis of Mitochondrial Genome Maintenance Protein 1 (Mgm1). *J. Biol. Chem.* **287**, 40131–40139 (2012).

61. Frohman, M. A. Role of mitochondrial lipids in guiding fission and fusion. *J. Mol. Med.* **93**, 263–269 (2015).
62. Booth, D. S., Avila-Sakar, A. & Cheng, Y. Visualizing Proteins and Macromolecular Complexes by Negative Stain EM: from Grid Preparation to Image Acquisition. *J. Vis. Exp.* e3227 (2011).
63. Mastronarde, D. N. Automated electron microscope tomography using robust prediction of specimen movements. *J. Struct. Biol.* **152**, 36–51 (2005).
64. Zheng, S. Q. *et al.* MotionCor2: anisotropic correction of beam-induced motion for improved cryo-electron microscopy. *Nat. Methods* **14**, 331–332 (2017).
65. Rohou, A. & Grigorieff, N. CTFFIND4: Fast and accurate defocus estimation from electron micrographs. *J. Struct. Biol.* **192**, 216–221 (2015).
66. Zivanov, J. *et al.* New tools for automated high-resolution cryo-EM structure determination in RELION-3. *eLife* **7**, e42166 (2018).
67. He, S. & Scheres, S. H. W. Helical reconstruction in RELION. *J. Struct. Biol.* **198**, 163–176 (2017).
68. Kucukelbir, A., Sigworth, F. J. & Tagare, H. D. Quantifying the local resolution of cryo-EM density maps. *Nat. Methods* **11**, 63–65 (2014).
69. Jumper, J. *et al.* Highly accurate protein structure prediction with AlphaFold. *Nature* **596**, 583–589 (2021).
70. Pettersen, E. F. *et al.* UCSF Chimera—A visualization system for exploratory research and analysis. *J. Comput. Chem.* **25**, 1605–1612 (2004).
71. Liebschner, D. *et al.* Macromolecular structure determination using X-rays, neutrons and

electrons: recent developments in Phenix. *Acta Crystallogr. Sect. Struct. Biol.* **75**, 861–877 (2019).

72. Emsley, P., Lohkamp, B., Scott, W. G. & Cowtan, K. Features and development of Coot. *Acta Crystallogr. D Biol. Crystallogr.* **66**, 486–501 (2010).
73. Williams, C. J. *et al.* MolProbity: More and better reference data for improved all-atom structure validation. *Protein Sci.* **27**, 293–315 (2018).
74. Pettersen, E. F. *et al.* UCSF ChimeraX: Structure visualization for researchers, educators, and developers. *Protein Sci.* **30**, 70–82 (2021).
75. Schindelin, J. *et al.* Fiji: an open-source platform for biological-image analysis. *Nat. Methods* **9**, 676–682 (2012).
76. Jurrus, E. *et al.* Improvements to the APBS biomolecular solvation software suite. *Protein Sci.* **27**, 112–128 (2018).
77. Krissinel, E. & Henrick, K. Inference of Macromolecular Assemblies from Crystalline State. *J. Mol. Biol.* **372**, 774–797 (2007).
78. Holm, L. & Rosenström, P. Dali server: conservation mapping in 3D. *Nucleic Acids Res.* **38**, W545–W549 (2010).
79. Nguyen, M. N., Tan, K. P. & Madhusudhan, M. S. CLICK—topology-independent comparison of biomolecular 3D structures. *Nucleic Acids Res.* **39**, W24–W28 (2011).
80. Fast, scalable generation of high-quality protein multiple sequence alignments using Clustal Omega. *Mol. Syst. Biol.* **7**, 539 (2011).
81. Robert, X. & Gouet, P. Deciphering key features in protein structures with the new ENDscript server. *Nucleic Acids Res.* **42**, W320–W324 (2014).
82. Ardail, D. *et al.* Mitochondrial contact sites. Lipid composition and dynamics. *J. Biol. Chem.* **265**, 18797–18802 (1990).

FIGURE LEGENDS

Figure 1 Human LACTB assembles into a filament. a, Domain organization of full-length human LACTB and the construct used in the study. The color scheme is used throughout the manuscript. **b,** Schematic diagram for recombinant expression and self-assembly of LACTB. **c,** Coomassie-stained SDS-PAGE of purified LACTB filament. **d,** Size-exclusion profile of wild-type (WT) LACTB using a Superose 6 column. SEC elution profile begins with the void volume (V_0) of the column. **e,** Representative negative-stain EM image of purified samples containing high molecular weight species. Negative-stain EM analysis is shown for the samples taken from the primary peak observed in size-exclusion chromatogram and are highlighted with a red box in **c**. Scale bar, 100 nm. **f,** Activity of the purified LACTB filaments determined by using a fluorescence-based assay with the error bars representing the standard error of the mean (s.e.m.).

Figure 2 CryoEM structure of human LACTB filament. a, CryoEM images of helical LACTB filaments were processed to obtain the 3D reconstruction of the polymer. LACTB protomers are colored differently, and filament rise, and twist are indicated. **b,** Top view of the LACTB assembly with the indicated filament width and inner lumen diameter. **c,** Ribbon diagram of LACTB monomer. The chain is colored in a rainbow gradient from N-terminus (blue) to C-terminus (red). Secondary structure elements of one protomer are labeled. **d,** LACTB (residues 97-547) α-helices (cylinders), β-sheets (arrows), and loops (lines) are depicted in a topology diagram.

Figure 3 Structural characterization of LACTB dimerization interface. a, LACTB protomers (colored in green and lilac) form an antiparallel dimer as shown in ribbon representation. Residues that are critical for oligomerization are represented in sticks. Orange boxes indicate the position of dimer interface residues. **b,** Zoomed in view of the orange box in **a**, showing the interactions that stabilize the dimer formation. The polar and charge-charge interactions are indicated by black

and red dotted lines, respectively. **c,** Size-exclusion chromatography (SEC) elution profiles of wild-type (WT) and mutant LACTB. SEC elution profiles begin with the void volume (V_0) of the column. Fractions were analyzed by SDS-PAGE and peak fractions used in negative-stain EM analyses are highlighted with red boxes. Negative-stain EM images demonstrate the polymerization activity of WT and mutant proteins. Scale bars, 100 nm. **d,** Catalytic activity of key residues involved in dimerization. Enzyme activity was determined *in vitro* by using a fluorescently labeled substrate and three independent experiments were performed for each sample. Error bars represent the standard deviation.

Figure 4 Structural basis of LACTB filament assembly. a, Ribbon diagram of LACTB tetramer. LACTB protomers are colored in green (A), lilac (B), orange (C), and pink (D). Residues that are critical for oligomerization are represented in sticks. Purple and blue boxes indicate the position of the residues located at the polymerization interfaces 1 and 2, respectively. **b, c,** Zoomed in view of the purple and blue boxes in **a**, showing the interactions that facilitate the polymerization of human LACTB. The polar and charge-charge interactions are indicated by black and red dotted lines, respectively. **d,** Size-exclusion chromatography (SEC) elution profiles of wild-type (WT) and mutant LACTB. SEC elution profiles begin with the void volume (V_0) of the column. Mutations to residues that are located at the polymerization interfaces 1 and 2 impair filamentation. Fractions were analyzed by SDS-PAGE and peak fractions used in negative-stain EM analyses are highlighted with red boxes. Negative-stain EM images demonstrate the polymerization activity of WT and mutant proteins. Scale bars, 100 nm. **e,** Catalytic activity of key residues involved in filament formation. Enzyme activity was determined *in vitro* by using a fluorescently labeled substrate and three independent experiments were performed for each sample. Error bars represent the standard deviation.

Figure 5 LACTB filaments bind to cardiolipin-enriched liposomes. a, b, Negative-stain EM images of LACTB filaments in the presence of liposomes. LACTB filaments display different modes of membrane binding and form stable interactions with cardiolipin-enriched liposomes. Scale bar, 100 nm. **c,** Zoomed in views of the red boxes in **a**, **b**, **c**, and **d**, showing the details of protein-liposome interactions. **d,** A schematic diagram of filament-liposome interactions illustrating different membrane binding modes of LACTB filaments.

Figure 6 Mechanistic model describing LACTB assembly mechanism within mitochondria. After being imported to mitochondrial IMS, LACTB protomers assemble into antiparallel dimers. Subsequently, LACTB dimers interact through two polymerization interfaces, which allow the stacking of antiparallel dimers in a helical fashion and lead to the polymerization into micron-scale helical assemblies. Upon filament formation LACTB gains catalytic activity and filament elongation increases the catalytic efficiency of the enzyme.

SUPPLEMENTARY FIGURE LEGENDS

Supplementary Figure 1 CryoEM raw data and validation of the human LACTB filament. a, A representative cryoEM micrograph and (**b)** 2D class averages of the human LACTB filament. **c,** Slices through the unsharpened density map of the LACTB filament are shown in the top view. **d,** CryoEM map of human LACTB filament is colored according to the local resolution estimation calculated by ResMap. **e,** Fourier Shell Correlation (FSC) curve shows 3.1 Å global resolution (masked in purple and unmasked in orange) with the gold standard criteria (FSC=0.143). **f,** Euler angle distribution of the segments used in final 3D reconstruction.

Supplementary Figure 2 LACTB filament data processing strategy. Flow chart summarizing cryoEM image-processing workflow, including 3D classification and 3D auto-refinement, CTF refinement and Bayesian polishing.

Supplementary Figure 3 CryoEM map quality of the LACTB filament. a, Fourier Shell Correlation (FSC) curves for the final helical symmetry imposed (purple line) and C1 symmetry (blue line) 3D reconstructions. **b,** 3D Fourier Shell Correlation of the final cryoEM map.

Supplementary Figure 4 Comparison of the LACTB monomer with different structures of homologous proteins and sequence alignment with bacterial PBP-βL family of enzymes. a-d, Comparison of human LACTB monomer (green) with *S. aureus* ClbP protein (yellow, PDB ID: 4GDN), *P. abyssi* Pab87 peptidase (orange, PDB ID: 2QMI), *A. halodurans* penicillin binding protein (pink, PDB ID: 3TG9), and *B. anthropi* D-amino-acid amidase (purple, PDB ID: 2EFU). The root-mean-square deviation of each structure relative to the LACTB monomer is shown at the bottom. While most β-strands align well between human and bacterial proteins, the surrounding helices and interface forming loops show significant differences between these

structures. **e,** Sequence alignment of LACTB homologs and orthologs. Residues that form the dimerization interface and polymerization interfaces 1 and 2 are highlighted with orange, purple and blue boxes, respectively. Catalytic site residues are highlighted with an asterisk. Secondary structure elements shown above the alignment are generated from the human LACTB structure. Sequences were aligned using Homo Sapiens LACTB (Uniprot ID: P83111), *S. aureus* ClbP (Uniprot ID: Q7A3Q5), *P. abyssi* Pab87 peptidase (Uniprot ID: Q9V2D6), *A. halodurans* penicillin binding protein (Uniprot ID: Q9KAM0), and *B. anthropi* D-amino-acid amidase (Uniprot ID: Q9LCC8).

Supplementary Figure 5 Structure of LACTB catalytic site and multiple sequence alignment of mammalian LACTB homologs. a, Active site and ligand recognition of human LACTB. Ribbon diagram of a monomer is displayed in green and residues forming the catalytic site are shown as sticks. Boxed zoom images highlight the positions of the conserved residues that contribute to catalytic site formation. **b,** Surface electrostatic potential representation of the LACTB monomer. Positive and negative electrostatic potentials are shown in blue and red, respectively. The substrate binding cavity is highlighted with the red circle. **c,** Sequence alignment of LACTB homologs. Residues that form the dimerization interface and polymerization interfaces 1 and 2 are highlighted with orange, purple and blue boxes, respectively. Catalytic site residues are highlighted with an asterisk. Secondary structure elements shown above the alignment are generated from the human LACTB structure. LACTB sequences from Homo Sapiens (human; Uniprot ID: P83111), Pan troglodytes (chimpanzee; Uniprot ID: K7CYM3), Macaca mulatta (rhesus macaque; Uniprot ID: F7EXQ6), Mus musculus (mouse; Uniprot ID: Q9EP89), Bos taurus (cow; Uniprot ID: P83095), Equus asinus (donkey; Uniprot ID: UPI001D03C0DD), Puma concolor (mountain lion; Uniprot ID: A0A6P6HFT1), and Lontra canadensis (river otter; Uniprot ID: UPI0013F34634) are aligned.

Supplementary Figure 6 SDS-PAGE and negative-stain EM analyses of LACTB filaments in the presence of H_2O_2. a, Coomassie blue-stained SDS-PAGE gel of wild-type (WT) LACTB protein treated with increasing concentrations (0.1%, 0.5%, and 1.0%) of H_2O_2. Indicated concentrations of H_2O_2 were incubated with purified LACTB for 30 min prior to SDS-PAGE analysis. The left lane is the molecular weight standards, and their positions are indicated. **b,** Representative negative-stain EM micrographs of WT LACTB treated with varying concentrations of H_2O_2 for 30 min prior to grid preparation. Scale bars, 100 nm.

Supplementary Figure 7 Model of LACTB enables mapping the disease-associated mutations. a, A schematic representation of full-length LACTB architecture. Resides 1-68 contain the predicted mitochondrial targeting sequence (MTS), and residues 243-290 form the flexible loop region. Residues that are associated with various human cancers are highlighted with a red dashed line. **b,** Ribbon diagram of human LACTB tetramer. Protomers that form the tetramer are labeled A to D and colored as in **Fig. 4a**. Mutations localizing to oligomerization interfaces are illustrated as sticks. Inset windows show the close-up views of oligomerization interfaces containing disease-associated mutations. Orange, purple, and blue boxes indicate the dimer, polymerization interfaces 1 and 2, respectively.

Fig. 1

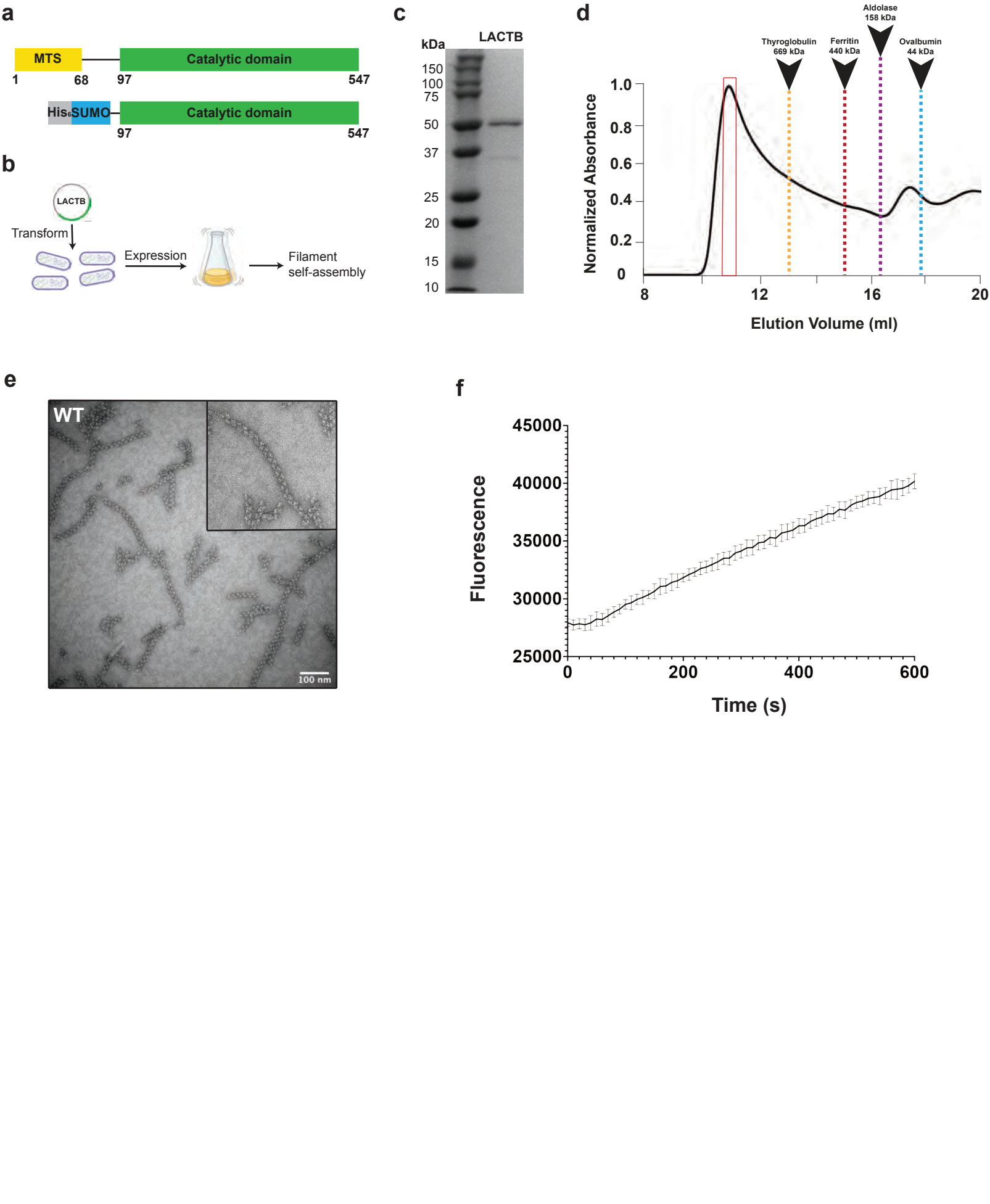

Fig. 2

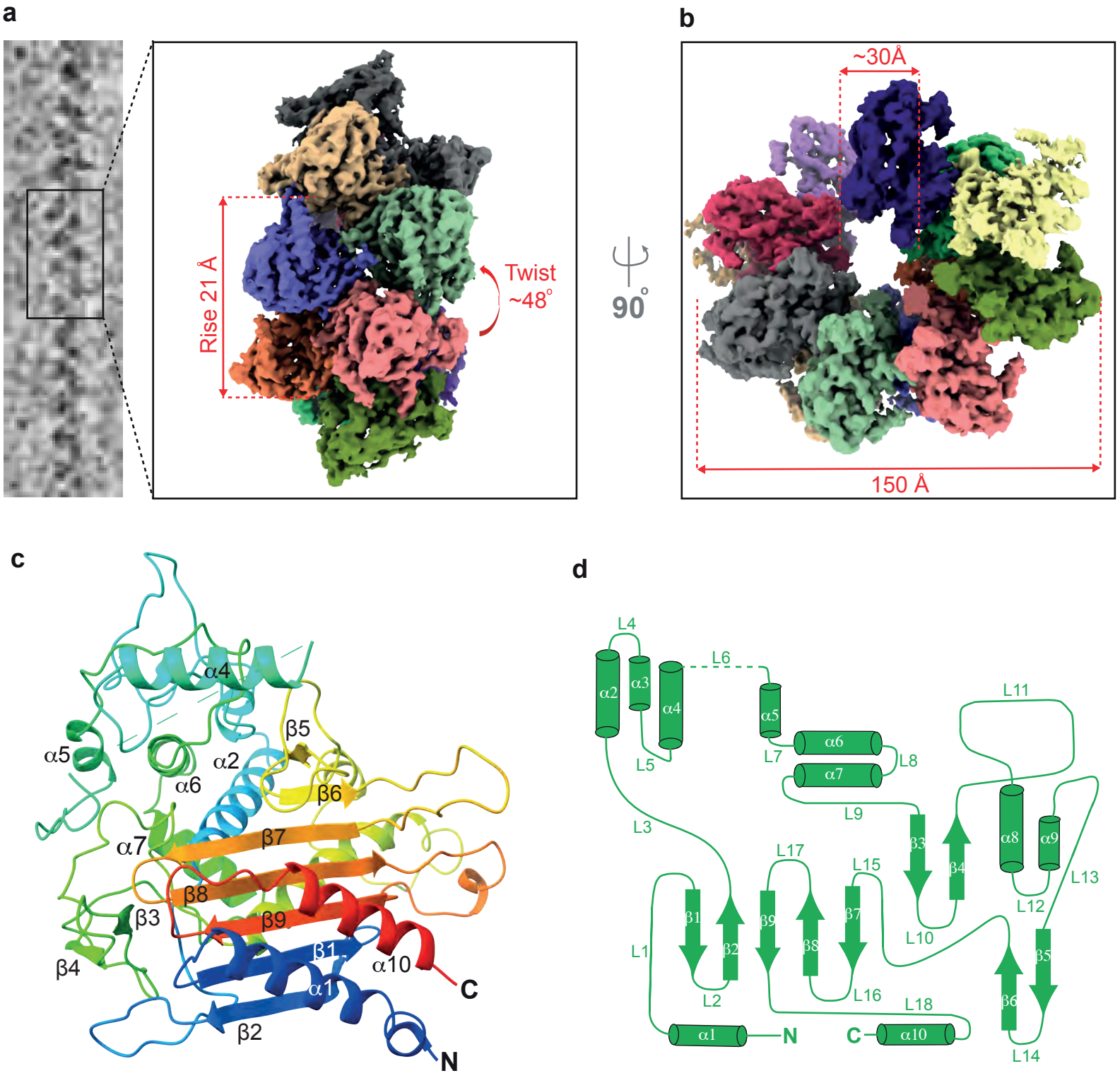

Fig. 3

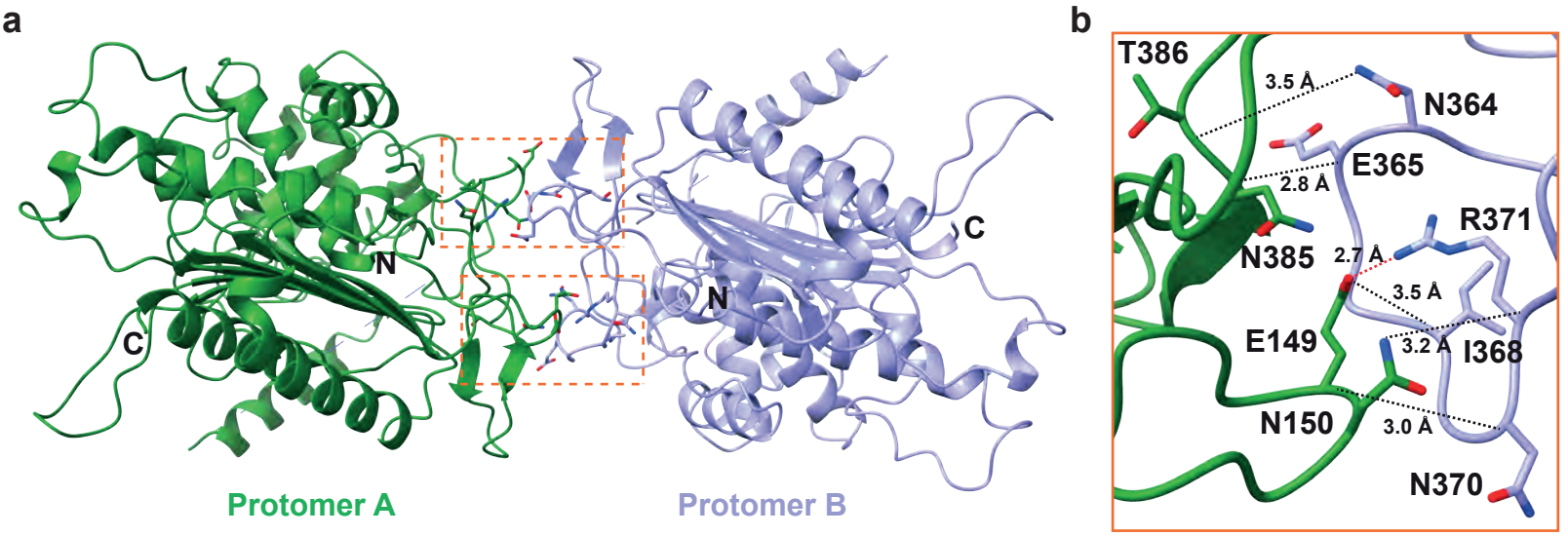

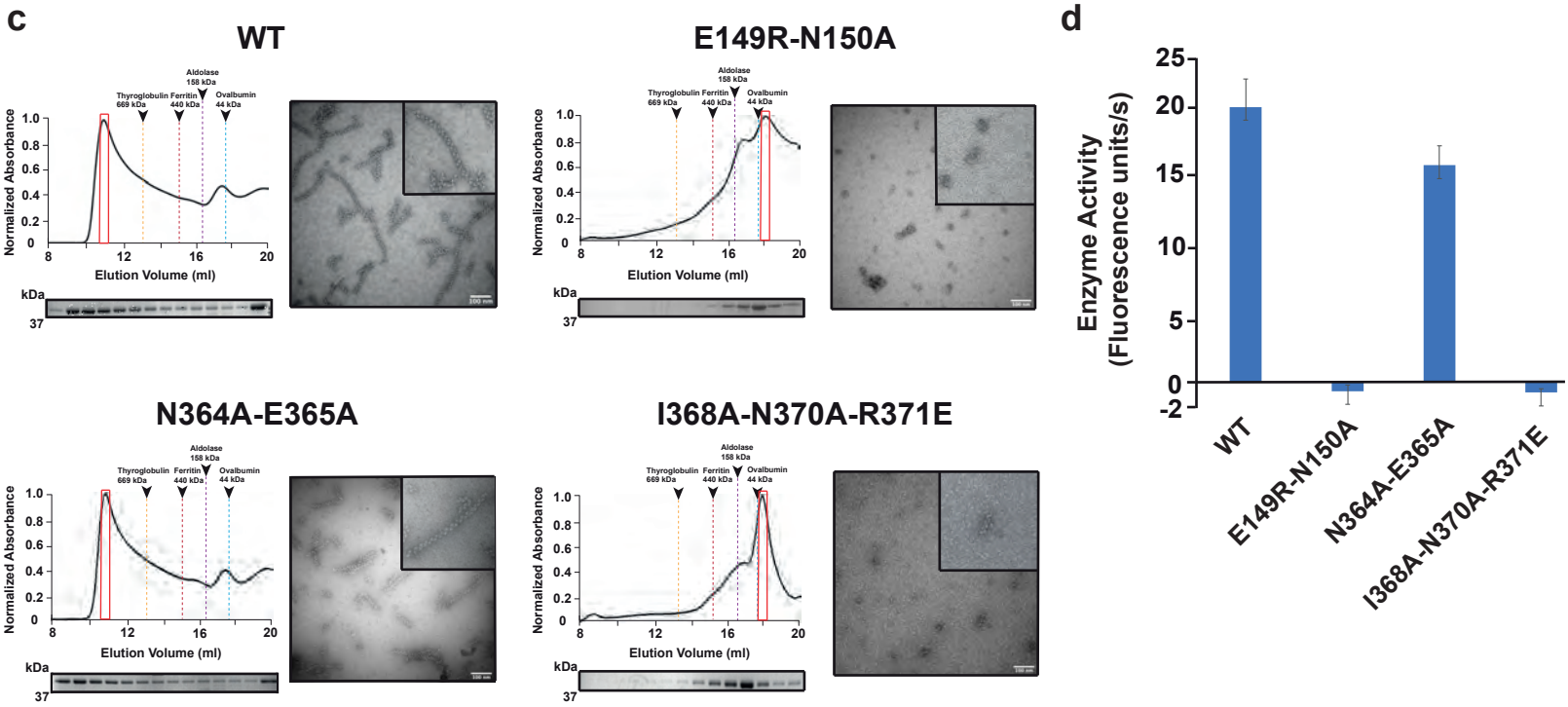

Fig. 4

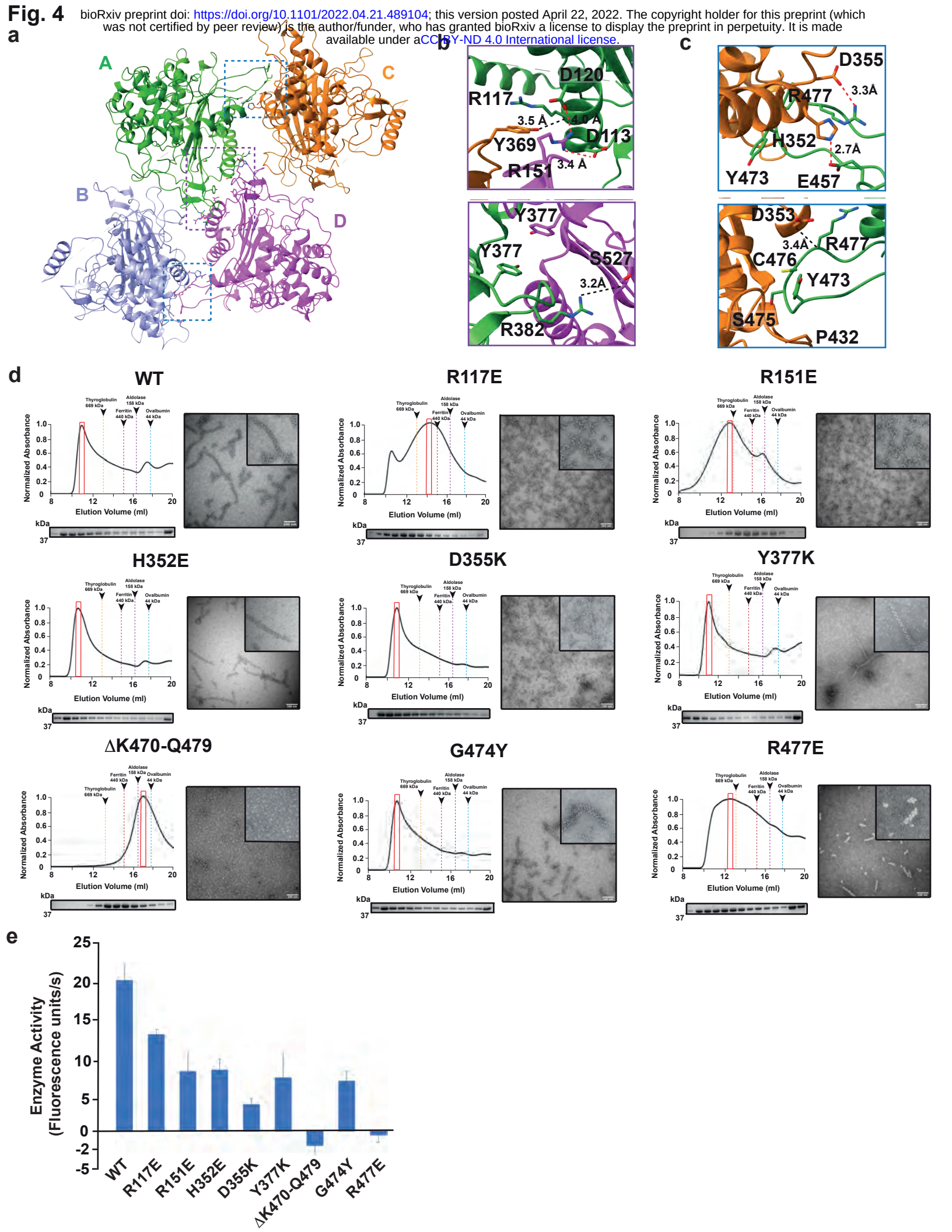

Fig. 5

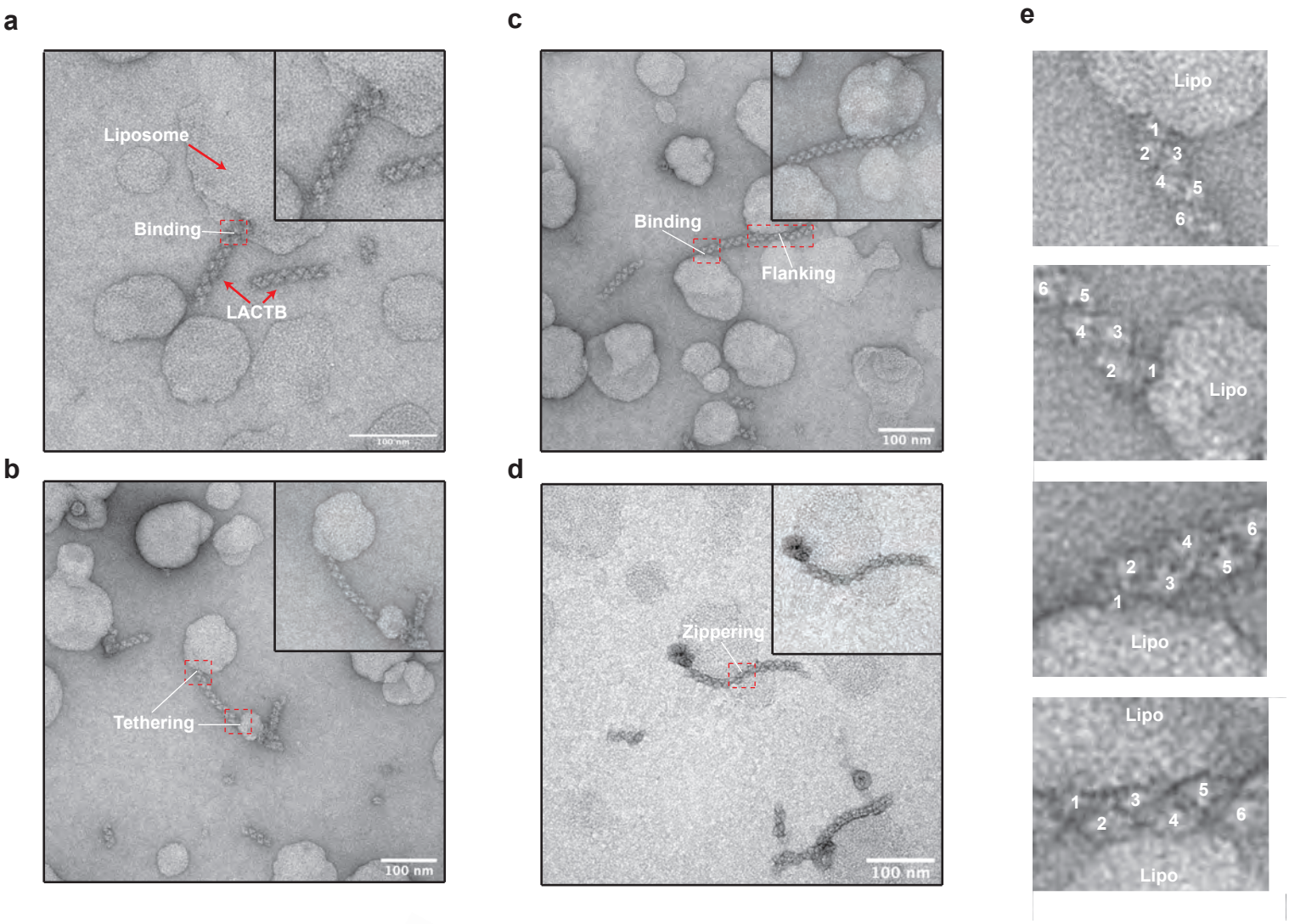

Fig. 6

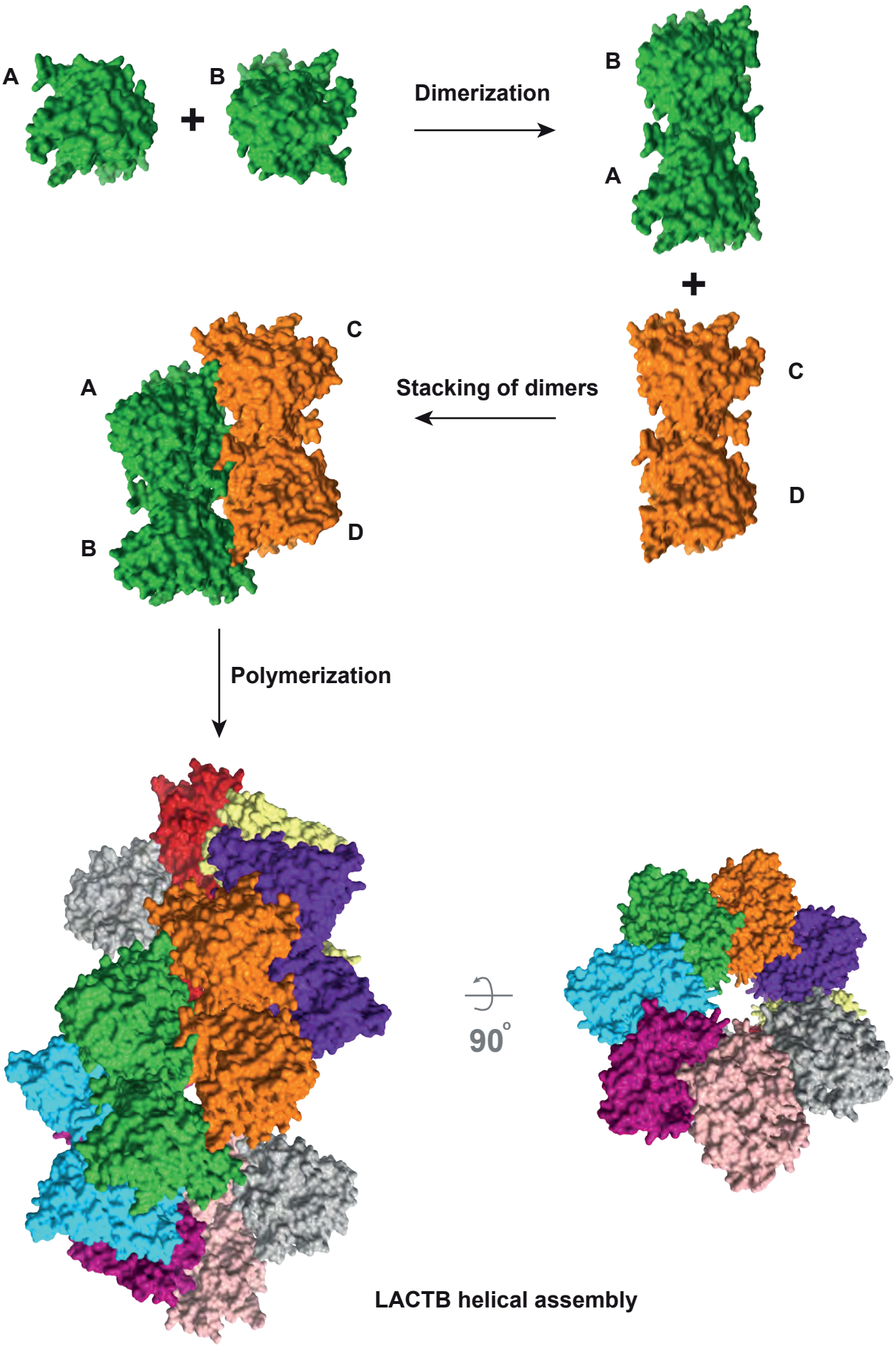

Table 1 | CryoEM data collection, refinement, and validation statistics

	Human LACTB (EMD-26595) (PDB 7ULW)
Data collection and processing	
Microscope	FEI Titan Krios
Camera	Gatan K3 Summit
Magnification	29,000x
Voltage (kV)	300
Electron exposure ($e^-/Å^2$)	65
Defocus (μm)	-0.5 to -1.5
Pixel size (Å)	0.8211
Symmetry imposed	Helical
Micrographs (no.)	7643
Initial segment images (no.)	430,592
Final segment images (no.)	248,548
Map resolution (Å)	3.09
FSC threshold	0.143
Map resolution range (Å)	3.1 to 5.8
Refinement	
Initial model used	*de novo*
Model resolution (Å)	2.84
FSC threshold	0.143
Map sharpening *B* factor ($Å^2$)	-87.6
Model composition	
Nonhydrogen atoms	18766
Protein residues	2400
B factors ($Å^2$) - min	
Protein	78.60
R.m.s. deviations	
Bond lengths (Å)	0.002
Bond angles (Å)	0.406
Validation	
MolProbity score	1.07
Clashscore	2.84
Poor rotamers (%)	0.00
Ramachandran plot	
Favored (%)	98.74
Allowed (%)	1.26
Disallowed (%)	0.00

Supplementary Figure 1

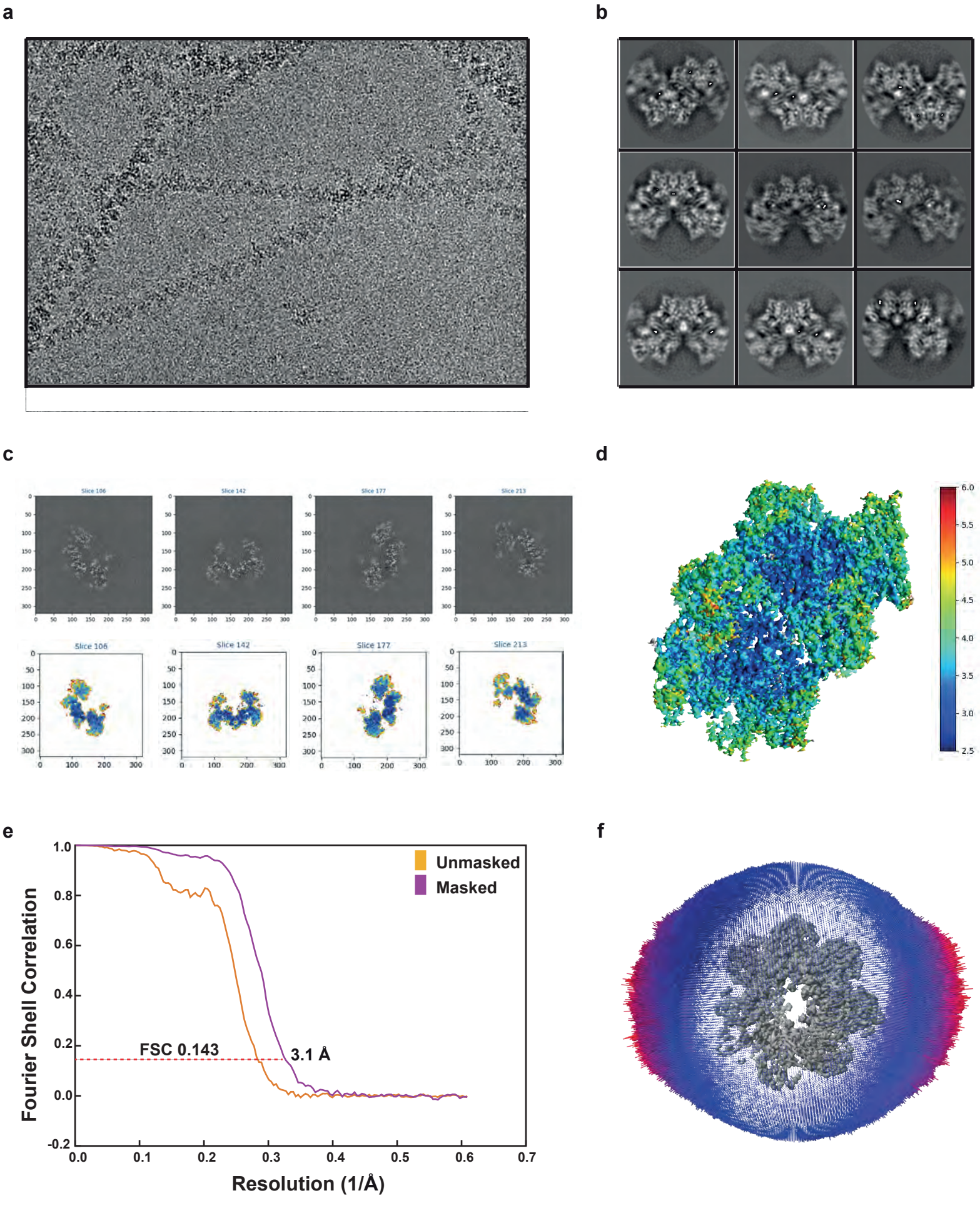

Supplementary Figure 2

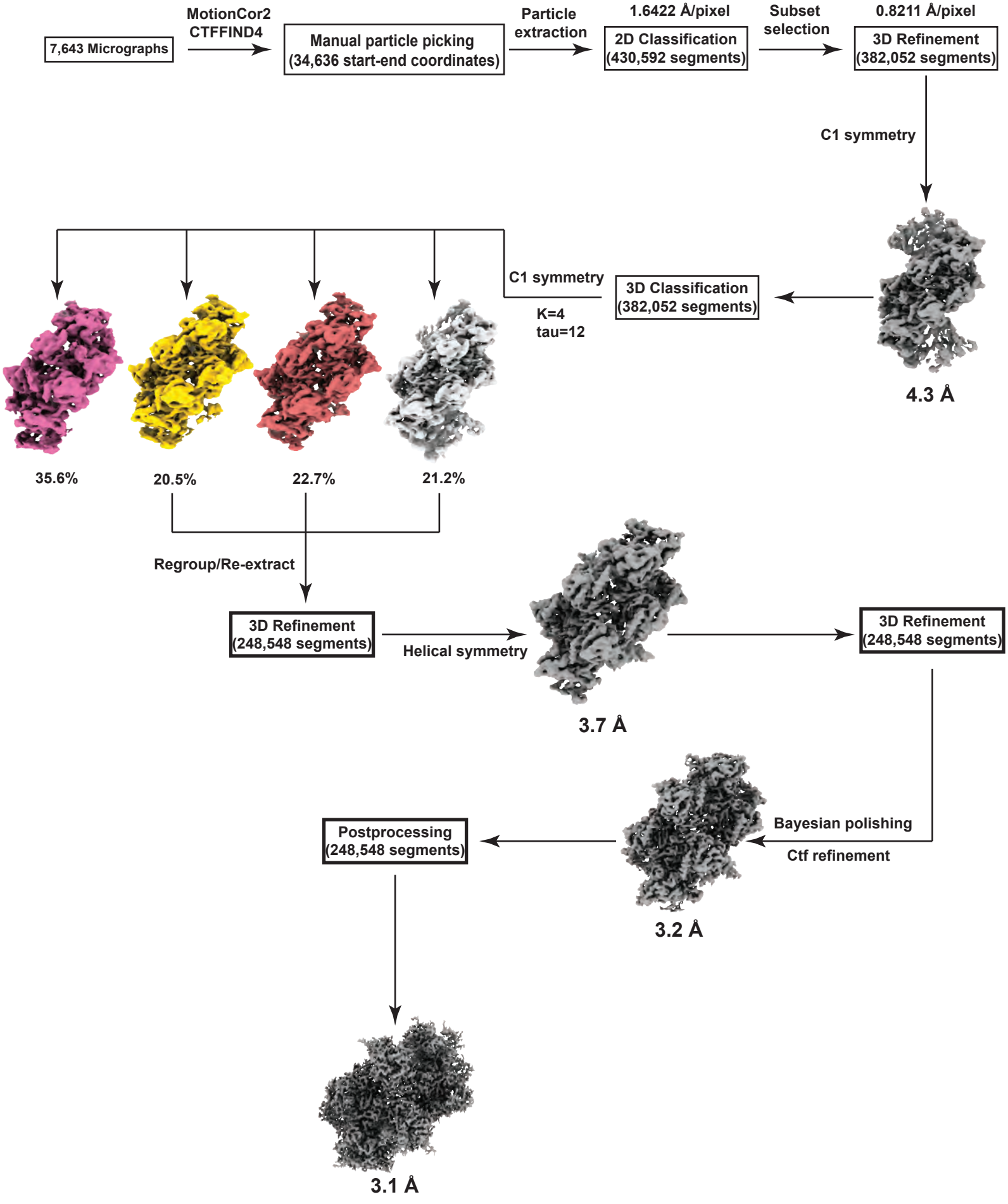

Supplementary Figure 3

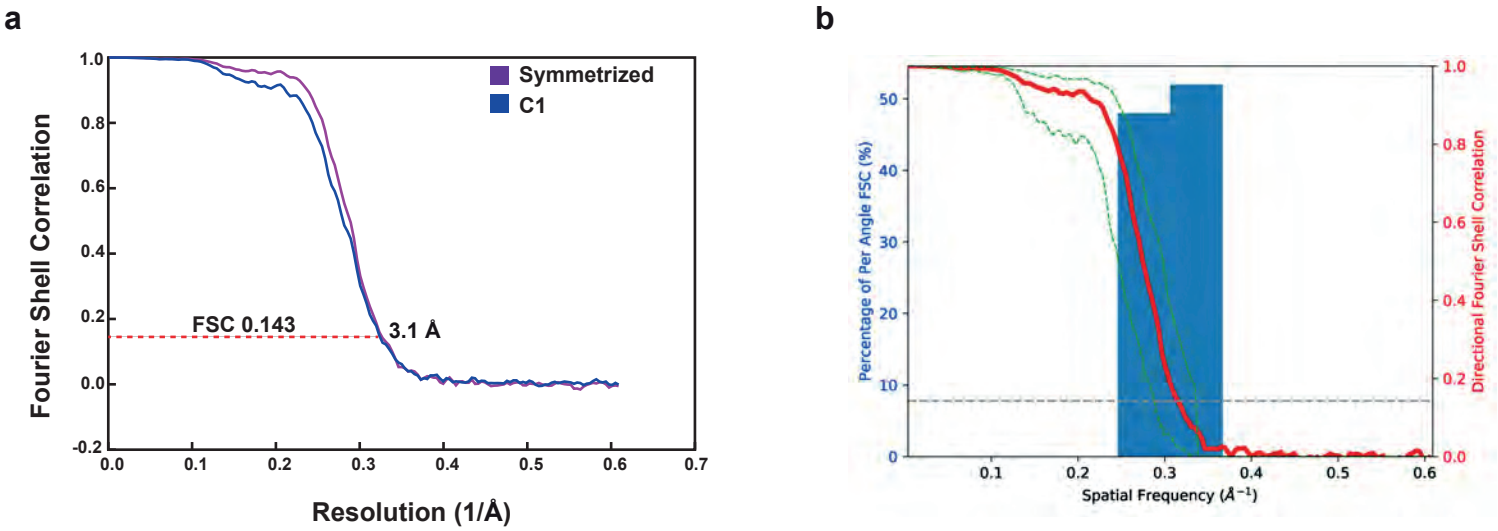

Supplementary Figure 4

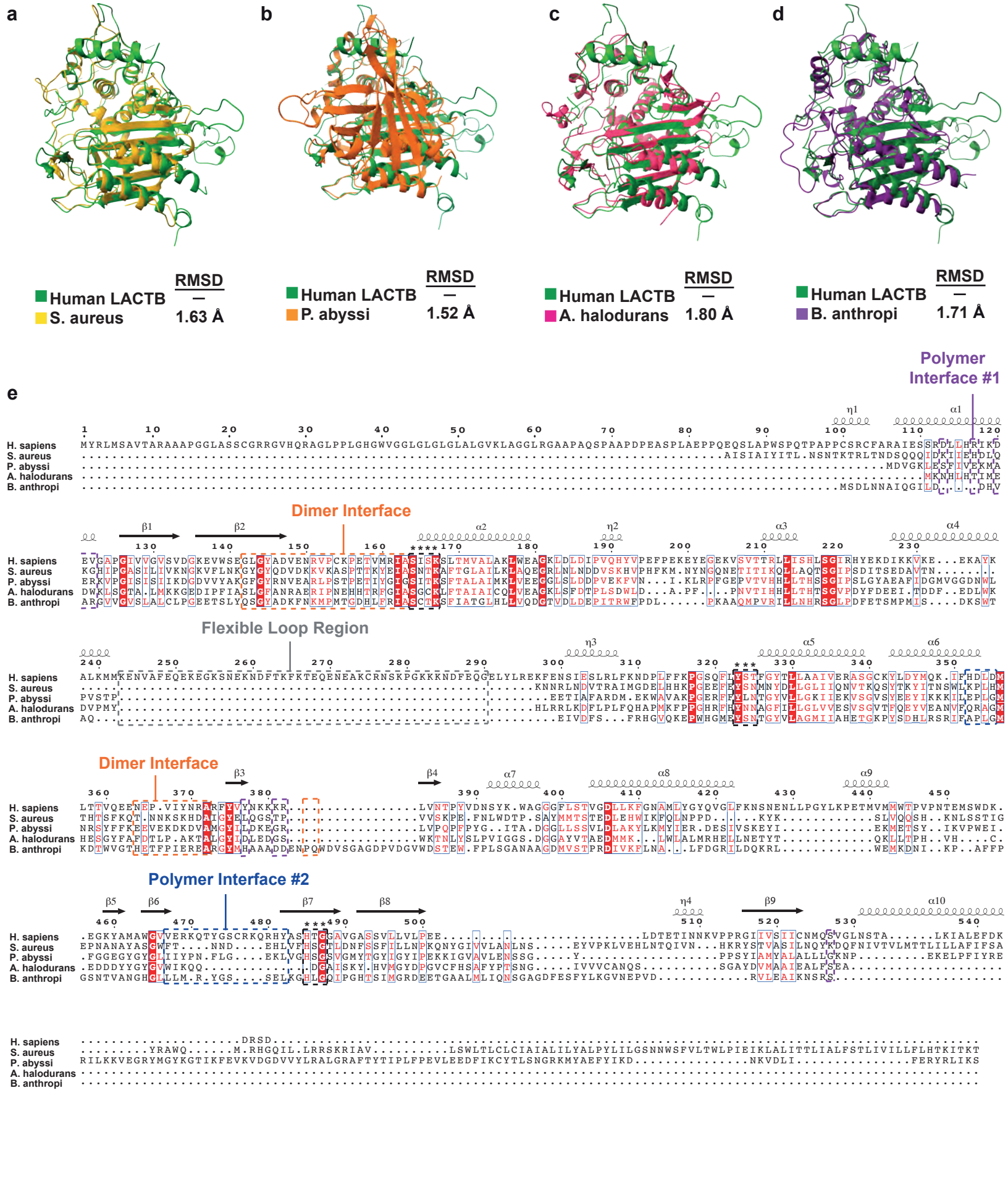

Supplementary Figure 5

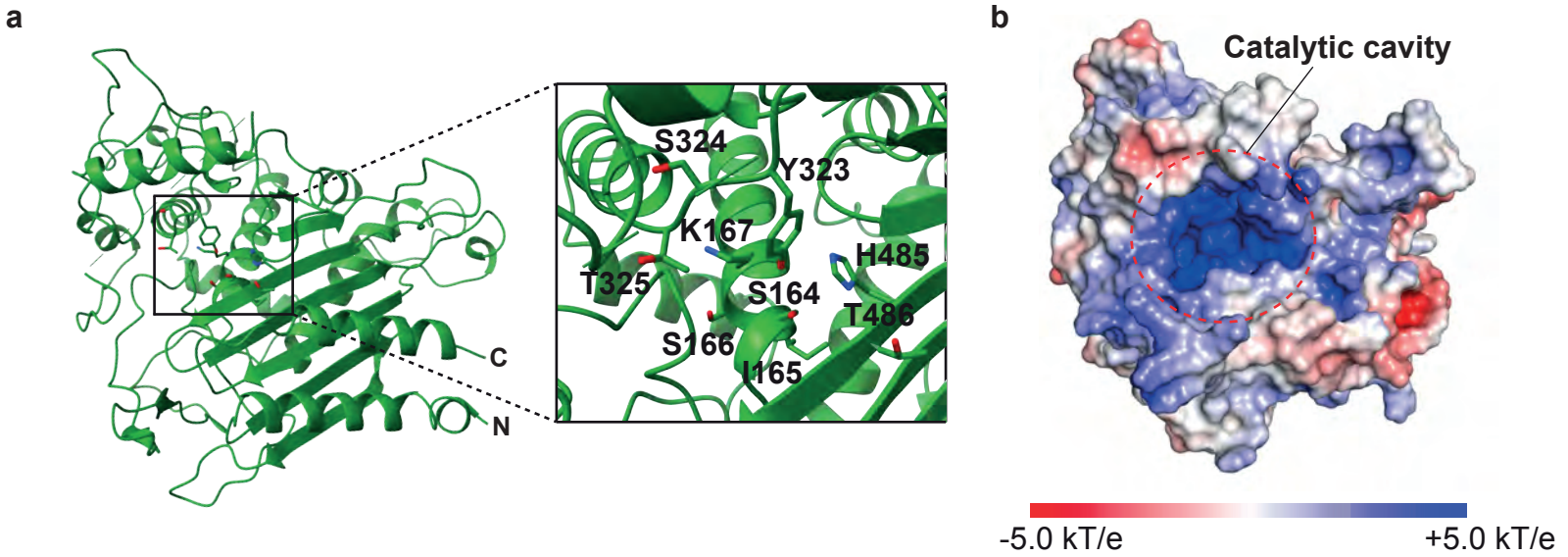

c

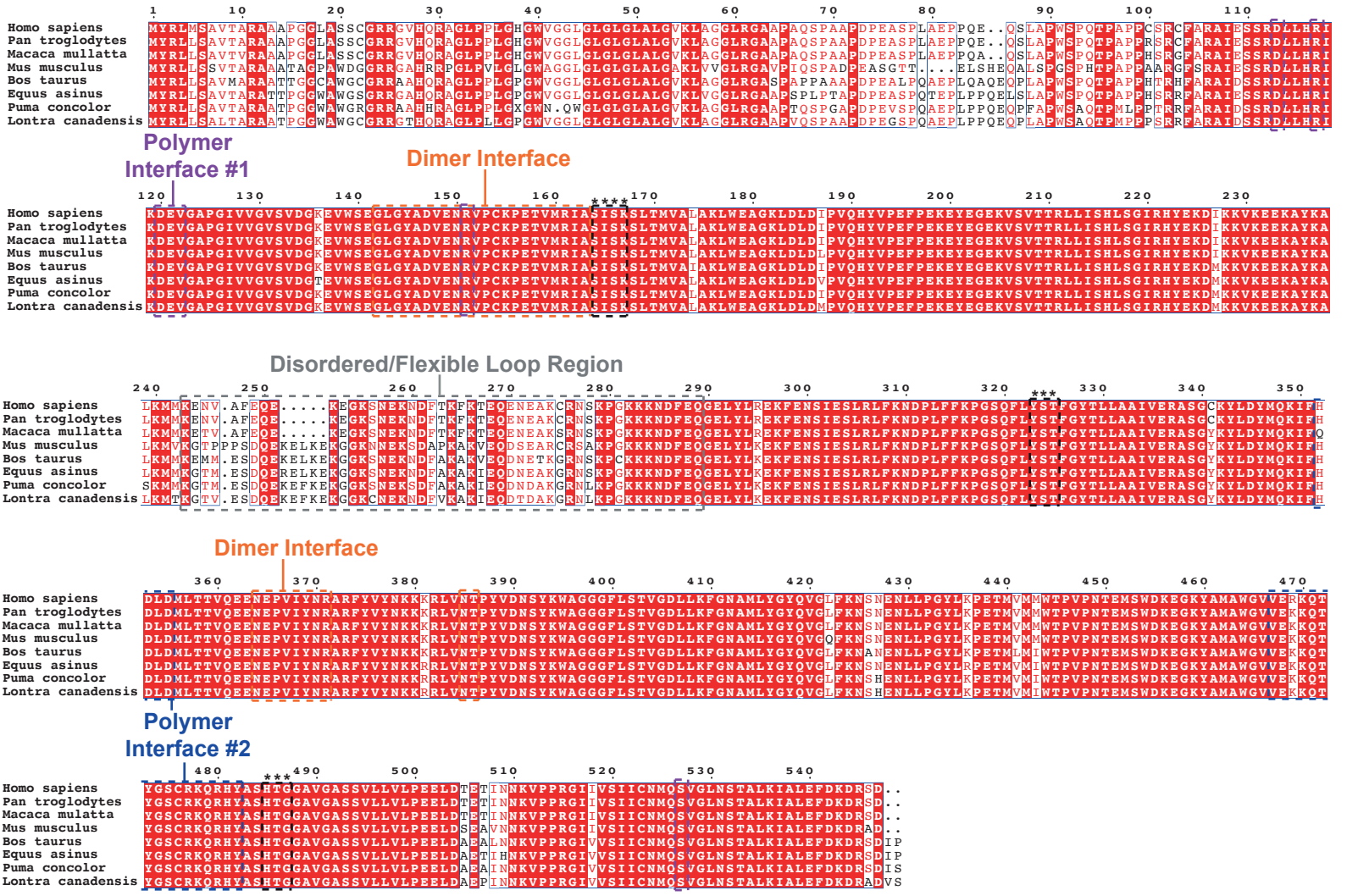

Supplementary Figure 6

a

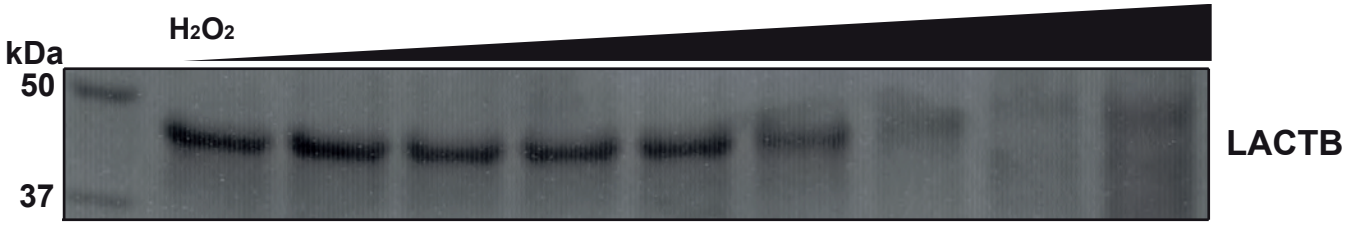

b

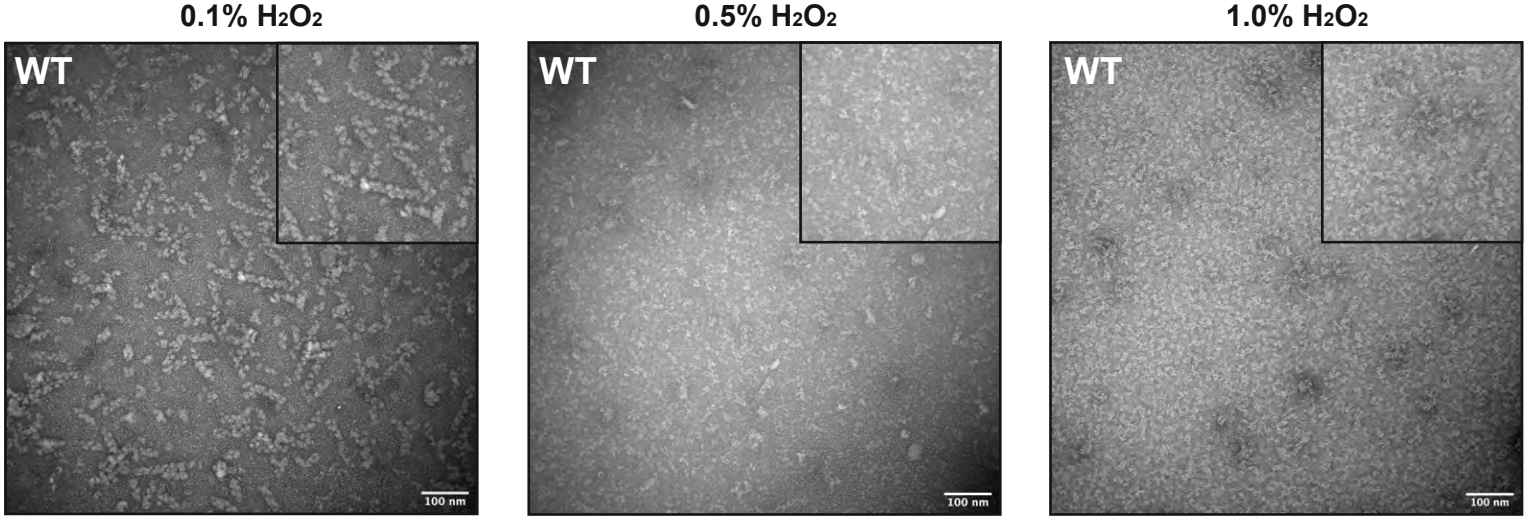

Supplementary Figure 7

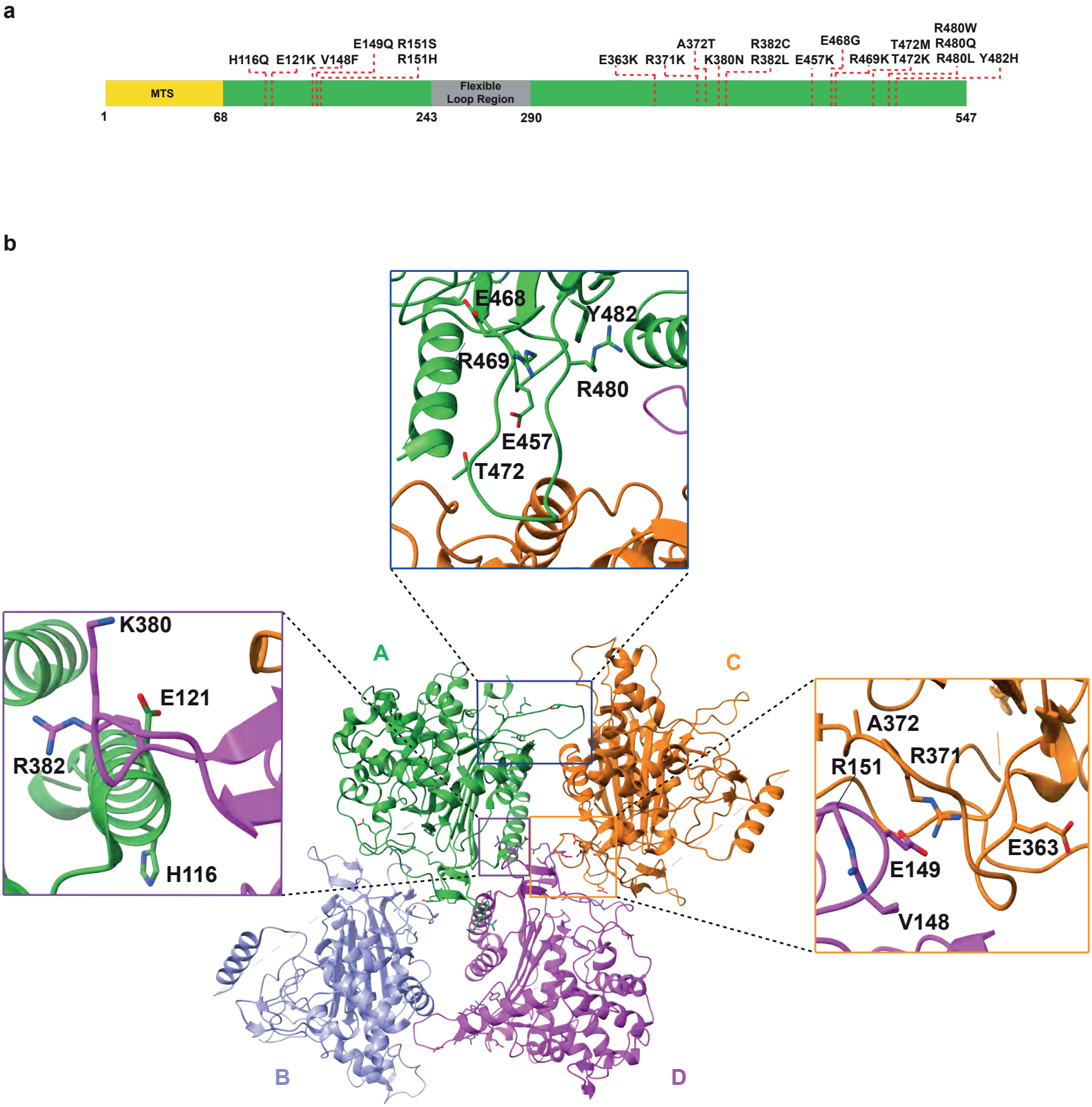

Supplementary Table 1 | Human LACTB mutations associated with cancer

Protein change	Clinical classification	Cancer type
H116Q	Neutral	Thyroid carcinoma
E121K	Pathogenic	Breast
V148F	Pathogenic	Kidney
E149Q	Pathogenic	Esophagus
R151S, R151H	Likely pathogenic	Uterus
E363K	Pathogenic	Pancreatic
R371K	Pathogenic	Lung
A372T	Pathogenic	Uterus
K380N	Pathogenic	Cervical
R382L, R382C	Pathogenic	Oral, uterus
E457K	Pathogenic	Bladder
E468G	Pathogenic	Glioma
R469K	Pathogenic	Colon, breast
T472K, T472M	Neutral	Melanoma, colon
R480W, R480Q, R480L	Pathogenic	Lung, colon, liver
Y482H	Pathogenic	Melanoma